The CB 244 Bok globule: protostellar outflow detection and detailed chemical characterization of proto- and pre-stellar regions

Tristan Vittoz[a], Eliot Raschetti[a], Hugo Derbey[a],
Supervised by: Dr. Ana López-Sepulcre[a,b], Dr. Romane Le Gal[a,b]

[a] *Univ. Grenoble Alpes, IPAG, F-38000 Grenoble, France*
[b] *IRAM, 300 rue de la piscine, F-38406 Saint-Martin d'Hères, France*

Abstract

We present a comprehensive study of the molecular content of the Bok globule CB 244, located at 200 pc and hosting a Class 0 protostar alongside a colder pre-stellar core. Using the IRAM 30 m telescope, we obtained 3 mm and 1 mm observations, targeting a wide range of molecular tracers including CO and its isotopologues, N_2H^+, SO, CS, CCS, CH_3OH, and various (nitrogen and carbon) bearing species.

Our observations led to the discovery of a protostellar outflow traced by CO molecule, and reveal clear chemical differentiation between the protostar and the pre-stellar core: rarer isotopologues ($C^{18}O$, $C^{17}O$) and molecules such as N_2H^+ and CCS probe the cold, dense, and chemically young gas of the pre-stellar core. Methanol emission reveals a secondary peak adjacent to the one associated with pre-stellar core, suggesting the presence of an additional dense structure and potentially a second site of star formation within the globule. In addition, the detection of sulfur-bearing species (SO, ^{34}SO) allowed us to trace the inner dense regions, revealing weaker emission toward the protostar compared to the pre-stellar core.

Our data provide a detailed characterization of the molecular budget of CB 244, offering new insights into the early chemical evolution of low-mass star-forming cores and the interplay between protostellar activity and cold gas reservoirs.

Keywords: Bok globules, Pre-stellar cores, Protostars, Molecular spectroscopy, Interstellar chemistry, Star formation

Contents

1. Introduction

CB 244 is a Bok globule located at a distance of ~ 200 pc, with an approximate extent of 0.5 pc (Stutz, A. et al., 2010). Bok globules are small, cold, and dense regions of the interstellar medium, rich in molecular gas and dust, observed as dark spots against bright backgrounds at optical wavelengths. These gravitationally bound structures are considered prime sites for low-mass star formation (Launhardt et al., 2010).

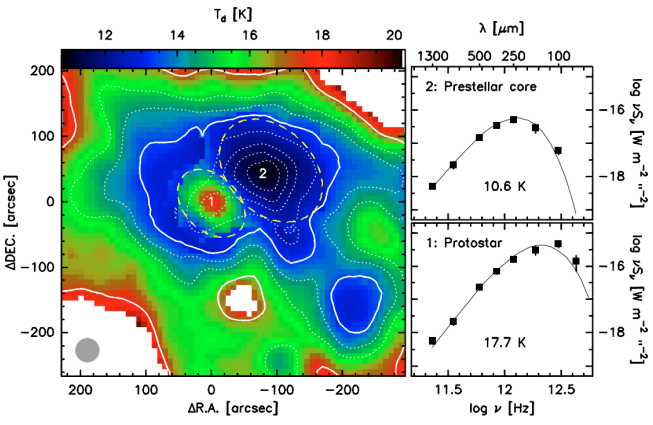

Figure 1: Dust temperature (color scale) and hydrogen column density (white contours) in CB 244 from Stutz, A. et al. (2010). The line-of-sight-averaged dust temperature was derived from modified black-body fits to Herschel PACS and SPIRE, Spitzer MIPS70, and ground-based extinction and sub-millimeter continuum maps at 0.8 and 1.3 mm. Column density contours are at 0.1 (thick), 0.3, 0.5, 1 (thick), 2, 3.5, 5, and 7×10^{22} H/cm^2, with the prestellar core peaking near 10^{23} H/cm^2. The locations of the Class 0 protostar ("1") and the prestellar core ("2") are indicated, with yellow dashed ellipses showing the areas used to compute source masses. The 37″ beam is shown as a grey circle.

As shown in Figure 1, CB 244 hosts two dense cores separated by ∼ 90″ (i.e., a projected distance of ∼ 0.09 pc at 200 pc): a pre-stellar core at 10.6 K and a low-mass Class 0 protostar at 17.7 K. The pre-stellar core represents a cold and quiescent phase of star formation, dominated by molecular freeze-out and early-stage chemistry, while the protostellar core is warmer and more evolved, where heating from the central object triggers complex chemical processes in its surrounding envelope (see Section 4).

Previous observations of CB 244 at millimeter wavelengths have revealed a chemically rich environment. The previous 2022 IRAM 30-m mapping run detected multiple molecular species, including methanol (CH_3OH) and carbon-chain molecules such as C_4H and c-C_3H_2. These molecules serve as tracers of different chemical regimes. For instance, the detection of iCOMs such as CH_3OH is a potential indicator of a hot corino (Ceccarelli et al., 2022), marking warm (>100 K) and dense zones where the sublimation of icy mantles creates a reservoir rich in complex organic molecules (Section 4.5). In contrast, carbon-chain species are often enhanced in various environments: they are abundant in cold cores during early evolutionary stages and in UV-illuminated regions, but they also characterize the lukewarm envelopes surrounding young protostars. In the latter case, this enhancement is a signature of Warm Carbon-Chain Chemistry (WCCC), triggered by methane sublimation at temperatures ≥ 30 K (Sakai and Yamamoto, 2013; Sakai et al., 2008).

Despite these results, several questions remain open. In particular, the presence of complex organic molecules (iCOMs) indicative of hot corino activity in the protostellar core (Zamirri et al., 2019) has not been confirmed in CB 244, and the physical and chemical structure of the pre-stellar core remains poorly constrained. Mapping additional transitions at 3 mm allows us to better characterize the spatial distribution and excitation of carbon-chain molecules, while single-point 1 mm observations provide access to higher-energy methanol and other iCOM transitions, potentially revealing the presence of compact warm gas around the protostar.

By combining these two observing bands, we adopt the following strategy: the 3 mm maps deliver large-scale spatial coverage over the entire globule, while the 1 mm observations achieve higher sensitivity for high-excitation transitions at the protostar location. This combined approach enables us to link the chemistry of the extended envelope to the processes occurring in the immediate vicinity of the protostar, and provides a first step towards a comprehensive astrochemical characterization of CB 244.

2. Observation

The observations were carried out with the IRAM 30 m telescope using the multi-band EMIR receiver coupled to the FTS200 digital spectrometers. Two frequency bands were employed, the 3 mm band (E0) and the 1.3 mm band (E2), each used with a different acquisition mode described below.

The observations were performed in dual-sideband heterodyne mode with EMIR. The sky signal is mixed with a local oscillator (LO) centered at a given frequency, shifting the sky frequencies to an intermediate frequency (IF). This conversion allows the simultaneous observation of the Lower Side Band (LSB) and the Upper Side Band (USB) on either side of the LO frequency. Each tuning covers an effective bandwidth of about 8 GHz per sideband, providing a wide spectral coverage around the selected central frequency and enabling the detection of several molecular transitions within a single setup.

The observing strategy was as follows: the 3 mm band was dedicated to extended spectral mapping of the globule, while the 1 mm band was used for deep integrations at a single position centered on the protostar. The program therefore consisted of an On-The-Fly (OTF) map together with a single-point integration at 1 mm.

The 3 mm band was used to map the spatial distribution of CB244. Observations were performed in OTF mode, in which the telescope continuously scans the region of interest while spectra are recorded, allowing homogeneous spatial coverage and more efficient acquisition than a mosaic of discrete pointings. The observed field includes both the protostar and the pre-stellar core. The data are organized as a three-dimensional cube (α, δ, ν), where the first two axes correspond to sky coordinates and the third to frequency (or equivalently Doppler velocity), thus providing one spectrum per spatial pixel (see Figure 2).

Mapping at 3 mm is favored by the better atmospheric transmission at these wavelengths. The lower opacity results in a more stable system temperature and allows longer integrations over extended areas without significant sensitivity loss, making large-scale maps more efficient in this band (Pardo et al., 2001).

In contrast, the 1 mm band was used exclusively in single-pointing mode, with the telescope fixed on the position of CB244-proto (the Class 0 protostar embedded in the CB244 Bok globule) during the full integration. This configuration provides a single spectrum within the telescope beam. This choice is driven by atmospheric and sensitivity considerations. Atmospheric absorption increases with frequency, mainly due to water vapor lines, leading to higher opacity and larger system temperatures at 1 mm. Extended mapping therefore becomes inefficient. In addition, transitions at 1 mm arise from higher excitation levels and are therefore preferentially excited in warm regions such as hot corinos, making this wavelength range particularly suitable for molecular detection. This is why this frequency band was chosen to observe the central warm protostar. Concentrating the integration time on a single position also improves the signal-to-noise ratio. The 1 mm data thus provide local spectral information complementary to the 3 mm maps.

All observations were performed in position switching (PSw) mode, alternating between the source position (ON) and a reference position free of emission (OFF). The ON–OFF subtraction removes atmospheric and instrumental contributions at the same observing frequency, directly isolating the astronomical signal. This mode was preferred over frequency switching or wobbler switching, which can introduce spectral distortions or self-subtraction effects for extended emission, respectively. PSw is therefore better suited to mapping relatively extended and line rich molecular clouds such as CB244.

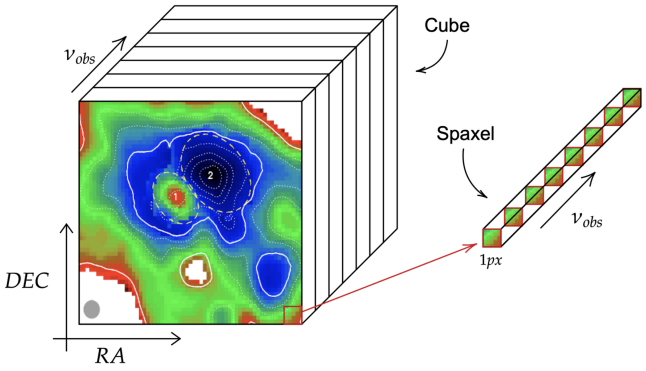

Figure 2: Schematic representation of a data cube. Different images of the same object are obtained at different observing frequencies. A "spaxel" refers to a spatial pixel extended over the full spectral (frequency) axis of the cube.

This efficiency-driven strategy combines extended spatial coverage at 3 mm with deeper, high-excitation spectroscopy toward the protostar at 1 mm, providing both large-scale spatial information and enhanced local spectral sensitivity.

Absolute intensity calibration was performed using the standard chopper-wheel method. This procedure relies on measurements of two reference loads at known temperatures (hot and cold loads) to determine the receiver gain and noise temperature. A sky measurement is then used to correct for atmospheric absorption. The spectra are calibrated in corrected antenna temperature T_A^* and can be converted to main-beam temperature $T_{\rm mb}$ using the telescope efficiency. This calibration accounts for receiver noise, atmospheric attenuation, and beam coupling losses (Ulich and Haas, 1976; Kutner and Ulich, 1981).

Regular pointing and focusing procedures were carried out throughout the observations to ensure stable gain and optimal beam coupling. Pointing was checked on bright compact sources (quasars or planets, depending on the day and time of our observation) to measure azimuth and elevation offsets, which were corrected before each observing sequence. The focus was also verified periodically, as defocusing directly degrades the effective beam size and sensitivity. These checks were repeated during the observing runs to compensate for thermal and mechanical variations of the telescope structure. Observations were preferentially conducted at sufficiently high elevations to minimize the atmospheric path length and thus reduce atmospheric absorption, which increases significantly at low elevation.

3. Data reduction

The data reduction was performed using `GILDAS IRAM` software, with the package CLASS. We first selected only the scans to consider for our data reduction with the help of TAPAS[1] (for Telescope Archive for Public Access

[1] https://tapas.iram.es/tapas/

System). Indeed, some scans were just used to do the calibration for example, while others were unusable due to excessive humidity or bad pointing (for the 3 mm observation we kept 22 scans over 30, and for the 1 mm, 32 over 32). Then we separated the four different frequency bands, namely the upper inner and outer, and the lower inner and outer.

The first part of the data reduction is common for the 1 mm and 3 mm. It consists of isolating a line. We start by performing a stitch, which is a simple mean of all the observations in a specific band. By doing so, we are able to reveal some emission lines that are not visible in a single observation. This mainly serves us to identify the frequency of the different lines. To perform this, we can zoom on a line and use the cdms (Müller et al., 2005) catalog to identify the name of the molecule that could emit it, its frequency, its upper level energy, its Einstein coefficient, and other spectroscopic properties. Once the line to be isolated in the stitched spectrum is selected, a frequency window (of $\sim$ 2 MHz width) is defined around it. The outer regions of this window define the area from which the continuum baseline is subtracted. This continuum is fitted using a first-degree polynomial, because it varies roughly as fluctuations around a linear function. The procedure to isolate a line works as follows, for each observation we:

- Create an output file were every reduced spectrum from each observation will be stored.
- Re-center the spectrum on the frequency of the line deduced from the stitch.
- Perform a spectral resampling on the velocity channel width, being careful to indicate a size in channels high enough so that the line is well resolved for the following studies. In this step, the line is isolated. The resulting resolution produces bins of ~ 0.2 km.s^{-1} in width.
- Subtract the continuum baseline with a first-degree polynomial outside the window defined previously to mask out the emission line.
- Convert the signal amplitude from T_a to T_{mb} to only have the measured intensity of the main beam. The Ruze law is applied to account for and correct efficiency losses caused by surface errors of the telescope.
- Switch the principal axis from frequency to velocity in order to facilitate the measurement of the Doppler effect and gas motions.

By stitching all the reduced output spectra, we obtain an isolated line with the background subtracted. For the 1 mm band, the reduction work ends here, and we can use the line to extract the physical parameters by fitting a Gaussian for example.

Concerning 3 mm band, we still have to build the moment maps. The first step consists in creating a cube of velocity-channel maps, taking care to properly orient the right ascension axis and to reframe the data in order to retain only the target map, excluding the reference position (see the previous Section 2 for the ON–OFF method). The noise is then estimated from a channel where no line emission is detected by taking the mean of the Gaussian distribution of each pixel value in this channel. Once this is done, only the channels containing line emission are selected (see the relevant channels used for each moment maps on the caption of their figure), and moment maps are constructed using a 3σ detection threshold. This procedure yields the integrated intensity (moment 0) map, the velocity field (moment 1) map, and the line width (moment 2) map. The final step consists of expressing the maps in relative coordinates.

4. Results for the 3 mm observations

In the following sections, we present the moment maps constructed from emission lines that were sufficiently strong in the 3 mm band. The list of detected molecular transitions and their spectroscopic properties is provided in Table B.2. Lines were considered as detected when their peak intensity exceeded a signal-to-noise ratio of 3σ in the resampled spectra. Line identification was performed primarily using the CDMS spectroscopic database, from which the vast majority of the transitions originate. Due to time constraints, a systematic cross-check with the JPL catalog was not carried out, and therefore some identifications should be regarded with appropriate caution.

4.1. CO molecule and isotopologues

From the 3,mm observations, the $J = 1 \rightarrow 0$ transition is detected for CO and its secondary isotopologues. The main isotopologue ^{12}CO is observed at a rest frequency of 115, 271.2 MHz, while ^{13}CO, C^{18}O, and C^{17}O are detected at 110, 201.4 MHz, 109, 782.2 MHz, and 112, 359.3 MHz, respectively, all within the $\sim$ 90–115 GHz atmospheric window. These transitions have low upper-level energies ($E_{\rm up} \lesssim 6$ K), making them easily excited in cold molecular gas. Their Einstein coefficients ($A_{ij} \sim 10^{-7}$–10^{-6} s^{-1}) correspond to moderate critical densities, so these lines efficiently trace the bulk molecular material. Owing to their different isotopic abundances, the set of CO isotopologues provides complementary sensitivity to a broad range of optical depths, from optically thick emission for ^{12}CO to progressively optically thinner tracers for the rarer species.

^{12}CO, the most abundant molecule in molecular gas after H_2, is very likely optically thick in both sources (top-left panel in Figure A.10). It nevertheless makes it possible to clearly identify a well-defined outflow, in particular through the moment-1 map (bottom-left panel in Figure A.10), which reveals the velocity structure of the moving gas. This constitutes, to the best of our knowledge, the first detection of a protostellar outflow in this source (we note, however, that spectra extracted at the positions of the blue- and red-shifted lobes would provide more robust evidence of the outflow; this analysis has not been performed here, as we do not yet know how to extract and present such spectra from the data cube). Its isotopologue ^{13}CO, on average about 60 times less abundant (Langer and Penzias, 1993), is also sensitive to the outflow (see Figure 4), while remaining almost undetectable in the two dense sources (see Figure 3), indicating that its emission there rapidly becomes too weak to emerge from the noise.

^{12}CO, the most abundant molecule in molecular gas after H_2, is very likely optically thick in both sources (top-left panel in Figure A.10). It nevertheless makes it possible to clearly identify a well-defined outflow, in particular through the moment-1 map (bottom-left panel in Figure A.10), which reveals the velocity structure of the moving gas (we note, however, that spectra extracted at the positions of the blue- and red-shifted lobes would provide more robust evidence of the outflow; this analysis has not been performed here, as we do not yet know how to extract and present such spectra from the data cube). Its isotopologue ^{13}CO, on average about 60 times less abundant (Langer and Penzias, 1993), is also sensitive to the outflow (see Figure 4), while remaining almost undetectable in the two dense sources (see Figure 3), indicating that its lines there rapidly become too weak to emerge from the noise.

The isotopologues C^{18}O (left panel in Figure A.10) and C^{17}O (middle panel in Figure A.10), approximately 500 and 2000 times less abundant than ^{12}CO (Wilson and Rood, 1994), are not detected in the outflow, but allow the dense sources to be traced. The C^{18}O emission is clearly detected toward both sources, while C^{17}O is strongly detected toward the pre-stellar core and only weakly detected toward the proto-stellar source (see Appendix B). This difference does not arise directly from the density of the medium, but primarily from the optical depth regime and excitation conditions of the lines.

Because of its high abundance, ^{12}CO rapidly becomes optically thick in dense regions (Pineda et al., 2008): its emission then probes mainly the outer layers of the gas, preventing direct access to the internal structure of the cores. In contrast, in the outflow, where the gas columns are lower and the kinematics are more pronounced, its emission remains easily detectable and constitutes an excellent tracer of the moving gas.

Conversely, rarer isotopologues such as C^{18}O and C^{17}O remain optically thin in dense cores, allowing them to trace the mass distribution and internal structure of these regions. In the outflow, however, the combination of their low abundance and the smaller column densities makes their emission too weak to be detected with the present sensitivity.

The weaker C^{17}O emission toward the proto-stellar source compared to the pre-stellar core likely reflects differences in excitation conditions. Pre-stellar cores are cold and characterized by low excitation temperatures, so that most of the population resides in the lowest rotational levels, making the $J = 1 \rightarrow 0$ transition relatively prominent. In contrast, in warmer proto-stellar environments, higher-excitation rotational levels become more significantly populated, which can reduce the relative intensity of the ground-state transition even if the total column density remains comparable or higher.

While this interpretation is consistent with standard expectations for molecular excitation in cold and warm environments, it should be regarded as a plausible explanation rather than a firm conclusion, since observational factors such as sensitivity limits, beam dilution, and source geometry may also contribute to the observed differences in line intensity.

4.2. N_2H^+ molecule

We detected the N_2H^+ line at 93173.398 ± 0.001 MHz in the 3 mm lower outer band. It has an energy $E_{up} = 4.5$ K and an Einstein coefficient of $A_{ij} = 3.63 \cdot 10^{-5}$ s^{-1}. The moment 0 and moment 1 maps are presented in Figures 6 and 7. We notice that N_2H^+ is present on the pre-stellar core but also on the protostar. The detection of this molecule toward both parts of the Bok globule CB244 traces colder and denser gas components of the system

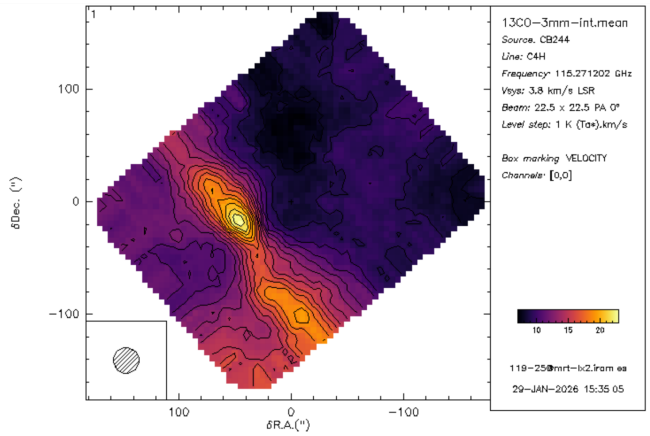

Figure 3: Moment-0 map of the ^{13}CO emission over the velocity interval 0.5–7.9 km.s^{-1}.

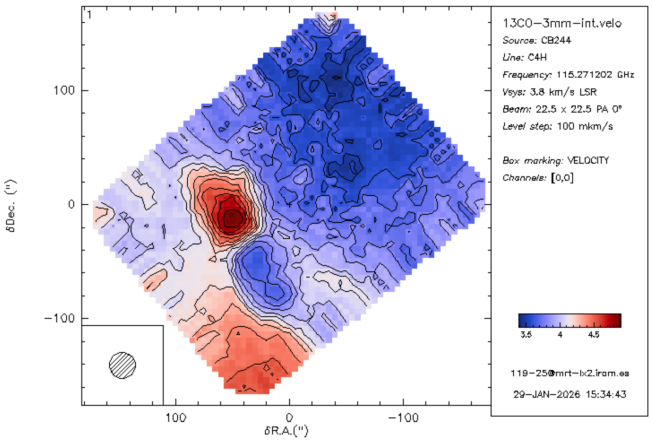

Figure 4: Moment-1 map of the ^{13}CO emission over the velocity interval 0.5–7.9 km.s^{-1}. The blue- and red-shifted lobes trace the high-velocity protostellar outflow, revealing the velocity structure of the gas.

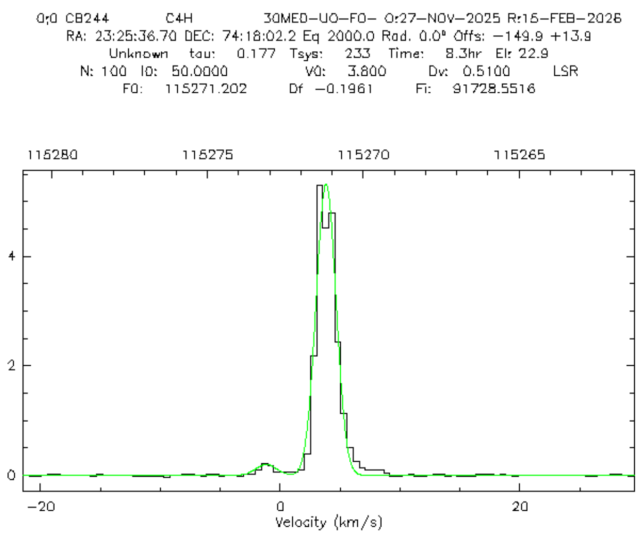

Figure 5: ^{13}CO lin fitted with a two-Gaussian function. The two Gaussian components can be interpreted as the blueshifted and redshifted parts of the same spectral line. The results of the fit are in Table B.3.

(Caselli et al., 2002). In the prestellar core, the presence of N_2H^+ is consistent with strong CO depletion, which freezes out onto dust grain mantles at low temperatures, allowing N_2H^+ to survive and become abundant in the gas phase. This confirms the chemically young and cold nature of the core because if the region were more evolved and therefore warmer, CO would have returned to the gas phase and efficiently destroyed N_2H^+ (Ceccarelli and et al., 2023).

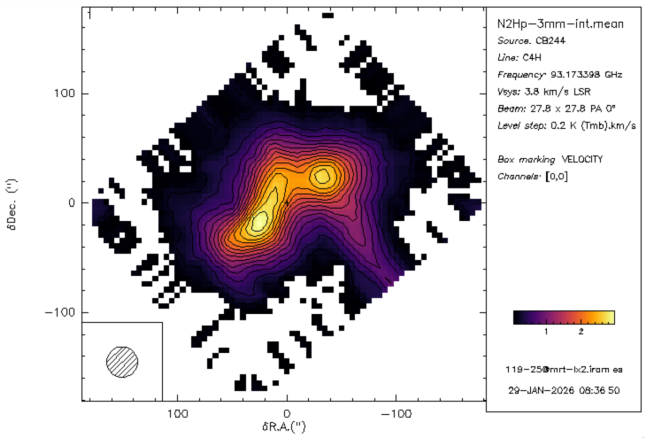

Figure 6: N_2H^+ moment 0 map. The protostar and the prestellar core can be easily distinguished.

Additionally, a N_2H^+ emission is also detected toward the protostellar source, despite the presence of the CO outflow revealed in the previous section. This could indicate that a significant fraction of the protostellar envelope remains cold and then might be shielded from protostellar heating outflow. While CO efficiently traces a dynamically perturbed and a bit warmer gas associated with outflows, N_2H^+ preferentially traces the more "inactive" dense material in the coldest innermost regions, where CO can still be depleted (Ceccarelli and et al., 2023).

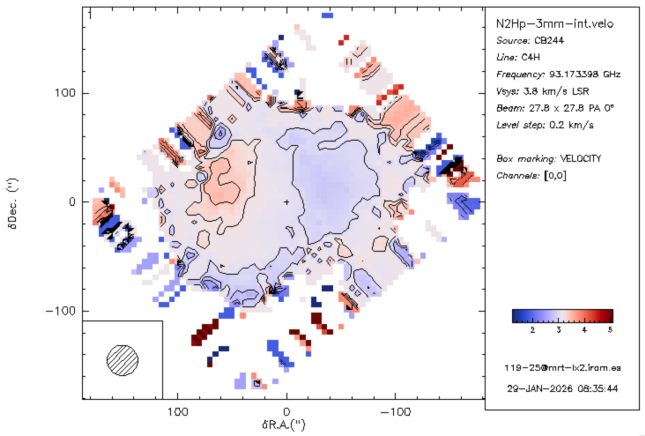

Figure 7: N_2H^+ moment 1 map. A blueshifted region is observed toward the prestellar core, while a redshifted region appears above the protostar; however, the signal is not strong enough to draw firm conclusions.

The coexistence of CO emission tracing the outflow and N_2H^+ emission tracing cold gas (Caselli et al., 2002) highlights a certain chemical differentiation within the system. This may indicate an early evolutionary phase where protostellar feedback is starting to affect the surrounding medium, while cold, dense gas reservoirs are still maintained both in the pre-stellar core and within the protostellar envelope.

4.3. SO molecule

From the 3*mm* observations, the SO molecule and its isotopologues, ^{34}SO and S^{18}O, are detected in the *LI* and *LO* bands at rest frequencies of 99 299.9MHz, 97 715.3MHz, and 93 67.3MHz, respectively. The upper-level energies of these molecular transitions are relatively low, ranging from 8.7 to 9.2 K, indicating that these lines can be easily excited under cold, dense conditions. The Einstein A_{ij} coefficients of the observed transitions show that the lowest value corresponds to the S^{18}O transition ($A_{ij} = 9.34 \times 10^{-6}$ s^{-1}), while the other transitions have higher A_{ij} values (i.e. more probable).

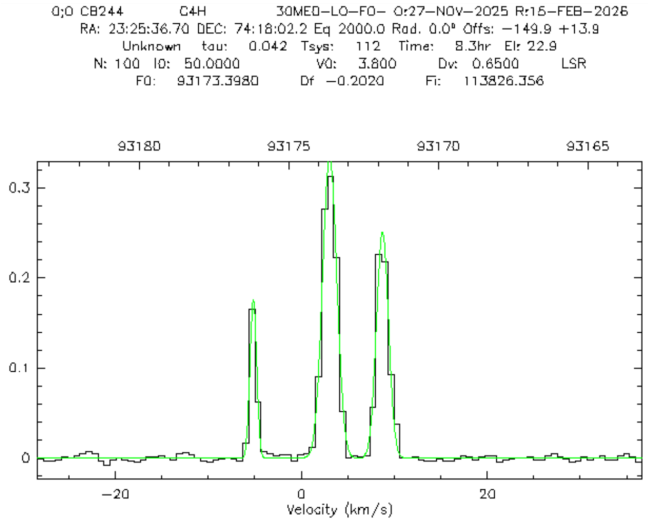

Figure 8: N_2H^+ line fitted with a three-Gaussian function. The thre Gaussian components can be interpreted as the hyperfine structure of the same spectral line. The results of the fit are in Table B.3.

All spectroscopic parameters used in this work, including the molecular species, the observational band, the frequency, the error on the frequency, the upper-level energy, the upper-level degeneracy, the Einstein coefficient, and the upper and lower energy levels, are listed in Table B.2.

The emission of sulfur-bearing molecules observed toward the pre-stellar core and the protostar highlights significant differences related to the physical and chemical conditions of these two objects (see Figure A.11). In the pre-stellar core, strong SO emission is detected (left panel in Figure A.11), along with a significant detection of its isotopologue ^{34}SO and, to a lesser extent, $S^{18}O$ (right and middle panels, respectively). The prominent presence of SO is consistent with the results of Herpin, F. et al. (2009), who showed that, although only a small fraction of the cosmic sulfur abundance is observable in cold and dense cores, simple sulfur-bearing molecules such as SO (or CS) can nevertheless be efficiently traced in these environments.
The simultaneous detection of ^{34}SO, which is less abundant but also less affected by optical depth effects, suggests that the SO column density in the pre-stellar core is sufficiently high to allow the detection of its isotopologues, while remaining in a regime where optical depth does not significantly hinder the observation of the main SO transition.

In contrast, the protostar exhibits rather diffuse SO emission with only marginal traces of ^{34}SO. The detection of SO and its isotopologues is overall unclear in this region, particularly for $S^{18}O$, which remains undetected. This can be explained by several factors. First, dynamical processes associated with the protostellar evolutionary stage, such as molecular outflows and enhanced turbulence, can disperse the dense gas and lower the local SO density within the telescope beam, thereby reducing the detectability of its emission. Second, chemical models and observations of more evolved cores indicate that SO is progressively converted into SO_2 through high-temperature neutral–neutral reactions, leading to a modification of sulfur-bearing molecular abundance ratios as evolution proceeds (Herpin, F. et al., 2009). However, this interpretation is debatable in our case, as no significant SO_2 emission was identified in our data, whether in the 3 mm spectral maps (Table B.2) or the deep 1 mm single-pointing (Table B.1). While this does not strictly rule out its presence, it indicates that SO_2 abundances remain below the detection threshold of the IRAM 30m telescope within our observed bandwidths.
As a consequence, SO may become less dominant in protostellar environments, while its isotopologues –already intrinsically less abundant due to the isotopic ratios of sulfur and oxygen– are expected to fall below the detection threshold.

More generally, SO and its isotopologues preferentially trace the inner regions and the dynamically active gas of prestellar cores, characterized by high densities and low temperatures. This is supported by their line widths, which are comparable to those of carbon-bearing molecules such as CO and CS (see Figures A.10 and A.12; Martinez et al. 2024), species that more efficiently trace the protostellar component. In the prestellar core observed here, these physical conditions appear sufficient to efficiently excite SO and its isotopologues. By contrast, within the protostellar source, the dynamical and chemical evolution of the environment likely leads to weaker, or even absent, emission from these species. Overall, these results are consistent with a scenario in which SO is abundant and readily detectable during the prestellar phase, but becomes progressively more difficult to observe at the protostellar stage.

4.4. CS molecule

During this campaign, we observed the CS molecule and its isotopologue $C^{34}S$ in the *LI* band, as well as the CCS molecule in the *LO* band, at rest frequencies of 97, 981.0 MHz, 96, 413.0 MHz, and 93, 870.1 MHz, respectively. The detected CS and $C^{34}S$ lines correspond to the $J = 2 \rightarrow 1$ rotational transition, that mean UL − LL = $2_0 - 1_0$, while the CCS emission arises from the $7_8 \rightarrow 6_7$ transition.
The upper-level energies of the observed transitions span a broader range than for SO, between 6.9 and 19.9 K, indicating that these lines can probe gas under a variety of excitation conditions, from cold dense material to slightly warmer environments. The associated Einstein coefficients are of the order of 10^{-5} s^{-1}, with the highest values corresponding to the most probable spontaneous transitions among the detected lines.
A detailed summary of the spectroscopic properties of the CS, $C^{34}S$, and CCS transitions is provided in Table B.2.

Similar to SO (see previous Section 4.3), the observations of CS in the protostar and the pre-stellar core reveal differences that reflect the physical and chemical conditions of these two objects. In the protostar, CS exhibits a pronounced peak, while diffuse emission is also detected around the source, extending toward the pre-stellar core.
According to Bulut, N. et al. (2021), CS is a widespread molecule that forms efficiently in dense molecular clouds. It remains chemically stable in these environments because they are shielded from UV radiation. However, in the coldest and densest regions, such as pre-stellar cores, CS can freeze onto dust grains (a depletion process), which significantly reduces its gas-phase abundance, as confirmed by our observations (left panel of Figure A.12). This molecule can be excited even at moderate densities ($n(H_2) \sim 10^4$–10^6 cm^{-3}), allowing it to trace dense gas. CS can also probe dynamical motions, particularly in structured flows that can be observed in the velocity maps of our observations (bottom left panel of Figure A.12). In addition, the presence of jets or shocks can release CS from dust grains, locally enhancing its gas-phase abundance and producing diffuse emission around the protostar, which could explain the CS ridge observed in our data, which appears to be co-located with the jet.

The isotopologue $C^{34}S$, which is much less abundant than CS, exhibits weak emission toward the protostar but shows a pronounced peak in the pre-stellar core. Unlike CS, its lines are optically thin, allowing a direct estimation of the gas column density without the effects of saturation. Consequently, $C^{34}S$ serves as a more reliable tracer of the densest and most compact regions of the core. Its emission is well correlated with that of dust and other dense gas tracers, such as HC_3N, confirming that it probes the inner zones of the core where CS is potentially optically thick and more difficult to interpret (Heithausen et al., 2008).

Finally, the CCS molecule exhibits different characteristics compared to CS and $C^{34}S$. According to Koley (2022), CCS is abundant during the earliest stages of core evolution, before the chemistry becomes dominated by nitrogen-bearing species such as NH_3. This is consistent with the fact that nitrogen-bearing tracers (e.g., NH_3, N_2H^+) are typically stronger toward denser, more chemically evolved material. This scenario is consistent with our observations, in which CCS is clearly detected in the pre-stellar core but is absent or only weakly present toward the protostar. This spatial distribution can be explained by the tendency of CCS to become depleted toward the densest and coldest dust peaks, where it adsorbs onto dust grains and is removed from the gas phase, remaining detectable mainly in the less dense outer envelopes of the core. In the vicinity of the protostar, higher temperatures (> 20 K) and the presence of shocks and outflows promote the destruction or chemical transformation of CCS into more stable or complex species, including sulfur-bearing molecules such as SO (see Section 4.3). Nitrogen-bearing species (e.g., NH_3) are not directly formed from CCS, but observations show an anti-correlation: CCS is typically stronger in the youngest, less dense regions, whereas nitrogen-bearing molecules are more abundant in denser, more chemically evolved material. Overall, these results are consistent with CCS being preferentially detected in the very early evolutionary phases of dense cores rather than in the more evolved protostellar stage.

4.5. CH3OH molecule

As part of these observations, methanol emission was observed toward CB244 in both the *LI* and *UI* bands. In the *LI* band, three closely spaced methanol transitions were detected at rest frequencies of 96,739.4, 96,741.4, and 96,744.5 MHz (central panel of Figure A.14). These lines correspond to the $2_{1,2} \rightarrow 1_{1,1}$, $2_{0,2} \rightarrow 1_{0,1}$, and $2_{0,2} \rightarrow 1_{0,1}$ rotational transitions, respectively (UL–LL), and arise from the torsional ground state ($v_t = 0$). The upper-level energies of these transitions span a range from $E_{up} = 7.0$ to 20.1 K, indicating that they are easily excited under cold and dense conditions.

The simultaneous detection of several transitions of the same molecule probing different excitation energies is particularly useful for constraining the physical conditions of the gas, such as the excitation temperature and the column density, for example through rotational diagram analyses, although such an analysis could not be performed in this work.

In addition, one methanol transition was detected in the *UI* band at a rest frequency of 108,894.0 MHz (left panel of Figure A.14), corresponding to the $0_{0,0} \rightarrow 1_{1,1}$ transition, also arising from the torsional ground state ($v_t = 0$). All relevant spectroscopic parameters of the detected methanol transitions are listed in Table B.2.

Observations of the CB244 Bok globule with the IRAM 30-meter telescope allowed us to detect two methanol (CH_3OH) transitions and to produce their integrated intensity maps (see the left and middle panels of Figure A.14 in Appendix A). These maps reveal clearly distinct spatial distributions within the pre-stellar core and the protostar. The first transition shows relatively diffuse emission, slightly enhanced toward the pre-stellar core, whereas the second transition exhibits a strong concentration at the pre-stellar core, with weaker emission near the protostar.

In pre-stellar cores, the central regions are extremely cold and dense, so that many molecules freeze out onto dust grains, forming thick icy mantles (Bergin and Tafalla (2007); Caselli and Ceccarelli (2012) and Ceccarelli et al. (2014)). Methanol, which has a relatively high binding energy to grain surfaces, would normally remain largely frozen in these cold regions. However, the strong emission observed toward the pre-stellar core (Saury et al., 2025) is likely due to excitation effects, as lower-energy transitions are more easily populated in the cold environment. In contrast, the interior of protostellar objects is sufficiently warm to sublimate methanol from the grains, but depending on the local conditions and the transitions observed, the gas-phase emission may appear weaker or differently distributed due to excitation and radiative transfer effects.

The spatial distribution of methanol can also be explained by its formation on icy mantles and by non-thermal desorption processes. According to Spezzano et al. (2016), mechanisms such as UV-induced photodesorption or cosmic-ray-induced desorption allow methanol to return to the gas phase, primarily in the outer layers of the core, which are less dense and slightly warmer than the central region where freeze-out dominates. This is consistent with the strong methanol emission we observe around the pre-stellar core.

Moreover, methanol is known to exhibit the highest level of deuteration among the molecules detected in pre-stellar cores (Nagaoka et al., 2005). During the pre-stellar phase, deuteration increases with core age and with the progression of CO freeze-out, which in principle allows deuteration measurements to be used as a temporal tracer of chemical evolution (Spezzano et al. (2016) and Marchand, P. et al. (2024)). However, once the protostellar phase begins, warmer temperatures can lead to a decrease in deuteration, potentially reversing this trend. This characteristic also explains methanol's detectability in the prestellar core and its relative absence near the protostar.

Finally, we note that, according to the central panel of Figure A.14, CH_3OH reveals a secondary structure adjacent to the core, which is the only feature shared with the first methanol transition (left panel of Figure A.14). This morphology could be explained if it indeed corresponds to the same object (core plus secondary structure), but a high opacity between the two regions appears to split the single core. Alternatively, this double structure also seems to be visible in the CS molecule (left panel, Figure A.12) and its isotopologue $C^{34}S$ (middle panel), which could suggest that it potentially corresponds to a second distinct prestellar core interacting with the first one. Given that the CH_3OH intensity of these two structures are similar, we could suggest that, if they are two prestellar cores, they exhibit a relatively similar level of chemical evolution, in agreement with our previous discussion.

4.6. Other nitrogen-containing carbon chemistry

In addition to the previous molecules found, we detected three nitrogen-bearing species. Their moment 0 and moment 1 maps are reported in Appendix A, Figure A.13.

The first molecule studied is HC_3N. It has been detected at a frequency of 109173.634 ± 0.010 MHz in the upper inner 3 mm band. The line has an upper-state energy of 34.1 K and an Einstein coefficient of 1.01×10^4 s^{-1}. HC_3N belongs to the family of unsaturated carbon-chain nitriles and can be associated with carbon-chain chemistry in cold and warm dense gas. Its detection in CB 244 is consistent with the carbon-chain richness previously reported toward this source, where several C-chain species have been identified in both the prestellar and protostellar cores by the previous 2022 master students. HC_3N is expected to be abundant where ion–molecule and neutral–neutral reactions efficiently build up unsaturated chains (Jørgensen, J. K. et al., 2004). Therefore, its emission should be complementary with N_2H^+, by tracing dense gas that can remain carbon-chain rich in regions that are not too hot. Its moment 0 maps, in the upper middle panel of Figure A.13, show the presence of HC_3N in both the protostar and the prestellar core, just as N_2H^+. This confirms the fact that these emissions are complementary. The presence of HC_3N on the protostar might also indicate that it is in an early evolutionary phase, where its temperature is still "cold". This conclusion is consistent with the one found in Section 4.2 for N_2H^+.

The second molecule found is CN. Its transition $v = 0, 1$ has been detected at multiple frequencies in the upper outer 3 mm band because of its hyperfine structure. To build the moment maps, we kept the most intense line, at 113499.644 ± 0.003 MHz. The line has an upper-state energy of 5.4 K and an Einstein coefficient of 1.06×10^5 s^{-1}. According to the study made by Jørgensen, J. K. et al. (2004), CN is expected to predominantly trace the less dense and more evolved regions of low-mass protostellar envelopes, rather than the coldest and densest gas. Also, CN is preferentially found in regions where CO remains largely in the gas phase, as opposed to dense and cold zones where CO is depleted onto dust grains. Therefore, we expect CN to be more abundant on the protostar than on the prestellar core. This is what we observe in Figure A.13, top left panel. Additionally, in Jørgensen, J. K. et al. (2004), it is shown that CN is found to be correlated with other nitrogen-bearing carbon-chain species such as HC_3N. Therefore, the presence of CN on the protostar could also be an explanation of the fact that we also find HC_3N in that region even if it is less cold than the prestellar core.

The last nitrogen-bearing molecule detected sufficiently powerful to build the moment maps is HNCO. It has been detected at a frequency of 109905.749 ± 0.007 MHz in the upper inner 3 mm band. The line has an upper-state energy of 15.8 K and an Einstein coefficient of $1.75 \cdot 10^{-5}$ s^{-1}. In Figure A.13, top right panel, HNCO is detected toward the presetallar core, while no significant emission is observed toward the protostar. This spatial differentiation suggests that HNCO predominantly traces the cold and dense gas. Marcelino, N. et al. (2010) showed that HNCO is found to be a tracer of dense gas across a wide range of physical conditions, from cold prestellar cores to warm protostellar envelopes and hot cores. Its abundance is best explained by a combination of grain-surface chemistry and subsequent non-thermal desorption, for example due to cosmic rays, making HNCO sensitive to regions undergoing gradual heating or chemical processing. One can imagine that this is the case in our system. The prestellar core could be gradually heated by the protostar and its outflow that are quite close. Therefore, HNCO, could be maintained in the gas phase by this gradual heating.

4.7. The strange unknown molecule

While reducing the data, we detected a quite powerful line in the 3 mm lower outer band, at ~ 91729 MHz. The only two molecules we identified for this line, with both cdms and in splatalog[2], are i-C_3H_7CN or $C_2H_3C_3N$. However, these molecules appear to contain too many carbon atoms bonded to other heavy atoms, such as nitrogen, to be present in our case. Therefore, we will classify it as a "unknown" molecule for the time, keeping in mind that these two molecules correspond to its emission frequency. The moment 0 and 1 maps are presented in Figure A.14, top and bottom right panel respectively. By looking at the moment 0 maps, we clearly see this molecules seems to trace the outflow. It has the same spatial distribution as the CO molecule. However, the velocity map of the molecule shows a similar structure to that of CO, but with reversed velocities, which is quite disturbing. In addition, the velocity range is larger than that of CO, which seems to indicate that this molecule reaches higher velocities and therefore could be lighter than CO. These unusual observational properties have led to it being nicknamed "The strange unknown molecule". A further examination (checked with the command `lid /i`) showed that the line is due to an image of the CO, v=0 line at 115271.202 MHz from the upper sideband because it is not possible

[2] https://splatalogue.online/#/advanced

to attenuate completely the opposite sideband. This can also explains the "reverse" velocity observed.

5. Results for the 1 mm observations

Single-pointing observations at 1 mm were performed towards the centre of the protostellar core in CB 244. The observations were carried out with the EMIR receivers connected to the FTS200 backends, covering the frequency ranges 213–221 GHz and 229–237 GHz. These tunings were selected to target several transitions of methanol (CH_3OH) with upper-level energies up to $\sim 90\ K$, as well as a set of complementary transitions of cyclopropenylidene (c-C_3H_2).

The primary goal of the 1-mm setup was to search for signatures of warm and compact gas associated with the protostellar core, in particular through the detection of high-energy methanol transitions, which are commonly used as tracers of hot corino emission. This is indeed the case, as we have detected two firmly identified methanol transitions at 1 mm, at 213,427.1 MHz in the LO band and 218,440.1 MHz in the LI band, corresponding to the $J_u - J_l = 1_{1,0,1} - 0_{0,0,1}$ and $4_{2,3,1} - 3_{1,2,1}$ transitions, respectively.

Due to the single-pointing nature of the observations and the limited signal-to-noise ratio achieved at 1 mm, no spatial information could be extracted from these data. The analysis therefore focused on the identification of spectral lines detected towards the protostellar position. In addition to several clearly identified CH3OH transitions, multiple lines of cyclopropenylidene (c-C3H2) were detected in both the LO and LI bands. These include the $33, 0–22, 1$ transition at 216,278.756 MHz, as well as the $60, 6–5_{1,5}$, $5_{1,4}–4_{2,3}$, and $5_{2,4}–4_{1,3}$ transitions at 217,822.148, 217,940.046, and 218,160.456 MHz, respectively, probing upper-level energies between ∼20 and 40 K. In addition, a number of weaker spectral features were detected that may correspond to other molecular species, potentially including interstellar complex organic molecules (iCOMs). In particular, a tentative detection of isopropyl cyanide (i-C3H7CN) is reported through the $167, 10–155, 11$ transition at 216,750.774 MHz (E_{up} = 56.2 K), although a firm identification will require additional observations.

Although we were not able to derive column densities at 1 mm, the detection of multiple methanol transitions with relatively high upper-level energies supports the presence of warm gas in the vicinity of the protostar. These results are consistent with the results inferred from the 3-mm observations and motivate future, more sensitive and spatially resolved observations at this wavelength, and a rotational diagram study.

6. Discussion of the results

The combined 3 mm mapping and 1 mm single-pointing observations show a clear physical and chemical differentiation within CB 244 between the Class 0 protostar and the nearby pre-stellar core. A key result is the identification of a protostellar outflow traced by ^{12}CO through its velocity structure. This is consistent with the high abundance of CO and its strong response to dynamically perturbed gas. The detection of ^{13}CO in the outflow further supports this interpretation, while its weak emission toward the dense cores suggests that the line becomes too faint (and possibly diluted by broader kinematics) to emerge significantly above the noise in these regions.

The distribution of CO isotopologues can be understood in terms of optical depth. In dense gas, ^{12}CO is expected to become optically thick rapidly, so its emission mainly probes outer layers rather than the inner structure of the cores. In contrast, rarer isotopologues such as $C^{18}O$ and $C^{17}O$ are less affected by saturation and therefore better trace the dense sources. This is consistent with our maps, where $C^{18}O$ traces both dense objects, while $C^{17}O$ is only detected toward the pre-stellar core. A plausible explanation is that the pre-stellar core combines higher columns of cold quiescent gas with narrower lines, which increases the peak brightness of such a rare optically thin tracer. Toward the protostar, broader lines and possible depletion or geometrical effects could reduce the peak intensity below detectability; however, this remains tentative given the sensitivity limits and beam dilution.

Dense and cold gas is also traced by N_2H^+, strongly detected toward the pre-stellar core, consistent with CO depletion in the coldest regions. Its detection toward the protostar indicates that a significant fraction of the protostellar envelope likely remains cold and dense within the beam, despite the presence of an outflow traced by CO. The CCS emission, prominent toward the pre-stellar core and weak toward the protostar, supports an evolutionary contrast: carbon-chain species such as CCS are typically enhanced in early-time chemistry and tend to decrease as the gas becomes warmer or more chemically processed.

Sulfur-bearing molecules show a similar differentiation. The stronger SO emission (and the detection of ^{34}SO) toward the pre-stellar core suggests that the corresponding column densities remain high enough to detect isotopologues, while the weaker emission toward the protostar may reflect a combination of beam dilution, dynamical disruption, and chemical evolution. In the same spirit, methanol is detected in several 3 mm transitions and peaks toward the pre-stellar core, consistent with efficient grain-surface formation and non-thermal desorption in cold dense gas. The methanol morphology also suggests a secondary structure adjacent to the core, although higher resolution and/or continuum constraints would be required to determine whether this corresponds to a distinct pre-stellar condensation.

Finally, the 1,mm single-pointing spectra toward the protostar provide access to higher-excitation methanol lines, supporting the presence of warmer gas in the protostellar environment. The detection of several CH_3OH transitions, and possible CH_3CHO lines, including transitions with relatively high upper-level energies, tentatively suggests the presence of a hot corino. However, the lack of spatial information and the limited signal-to-noise ratio prevent a quantitative characterization of the excitation conditions and thus a firm confirmation of this interpretation. Additional, deeper 1,mm observations and/or interferometric follow-up would be required to confirm these tentative identifications and to robustly constrain the abundance and excitation of complex organic molecules.

7. Conclusion and further work

Our observations of the Bok globule CB 244 provide a detailed view of its molecular content and early chemical evolution. We report the discovery of a protostellar outflow traced by optically thick CO, highlighting active feedback from the Class 0 protostar. The pre-stellar core exhibits cold, dense, and chemically young gas, revealed by tracers such as N_2H^+, CCS, and rarer CO isotopologues. Additionally, methanol emission hints at the presence of a possible secondary pre-stellar structure, suggesting that CB 244 may host multiple sites of star formation. Sulfur and carbon bearing molecules reveal clear chemical differentiation between the protostellar and pre-stellar regions, reflecting both the physical conditions and evolutionary stages of the cores.

Future work will focus on performing rotational diagrams for methanol and C-chain species to better constrain the excitation temperatures and column densities of both cores, especially using the 1 mm band. Our current data show that the detected methanol lines mainly trace cold gas, while higher-energy transitions detected at 1 mm (up to E_{up} = 45 K) support the presence of a hot corino in the protostellar core, providing a strong motivation for guiding future observations. Similarly, combining our current observations with those from 2022 likely provides enough transitions of c-C_3H_2 and C_4H to characterize the chemical budget and compare the evolutionary stages of the protostellar and pre-stellar cores. Finally, high-resolution mapping will still be essential to confirm the tentative secondary pre-stellar structure and to resolve the kinematics and morphology of the newly discovered protostellar outflow.

8. Acknowledgements

We would first like to thank Ana and Romane, who provided us with excellent training for observations at the IRAM 30 m telescope. They guided us efficiently through all stages of the observing process—from preparation, to execution, and data reduction—within a remarkably short timeframe and with great precision. This experience was not only scientifically enriching, but also a valuable human experience, thanks to their kindness and their genuine desire to share with us the adventure of traveling to Spain and conducting observations at a radio telescope.

We also wish to acknowledge two key contributors: Gabriel, the astronomer on duty, and Joaquín, the chief operator, who trained us in the practical operation of the telescope (and handled with unfailing calm all the alarms we inevitably managed to trigger along the way !). We further thank Frederico De Amor for a memorable encounter; he broadened our cultural knowledge of the city of Granada and generously shared his excellent company.

More broadly, we are grateful to the entire IRAM Spain team, as well as to our academic program for offering us this exceptional opportunity—one that very few students worldwide are fortunate enough to experience.

Figure 9: Dream team picture.

Appendix A. Maps

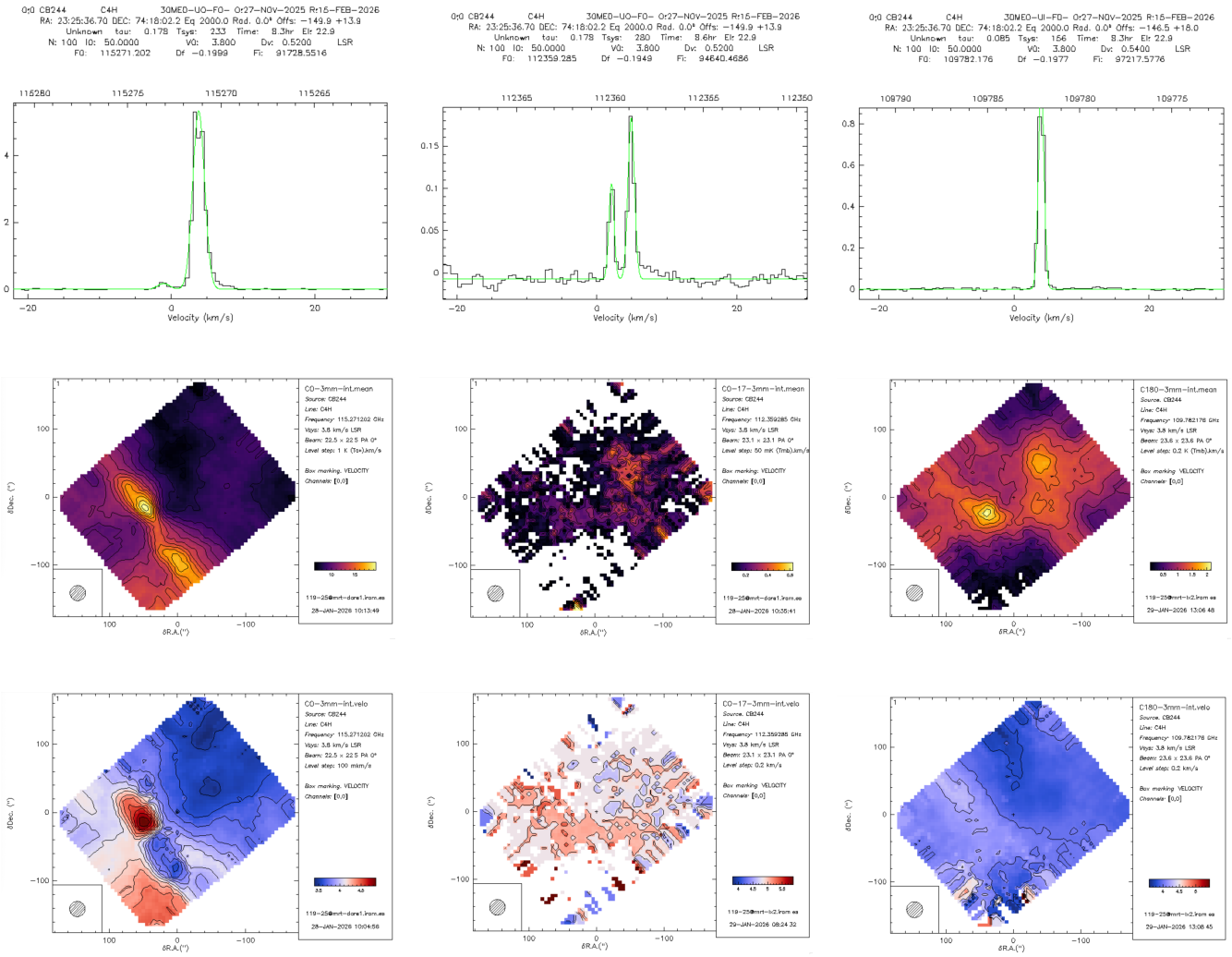

Figure A.10: The top panel shows the line with Gaussian fits and some information about the data. In the left figure, one can see the presence of an outflow by looking at the red and blue shifted parts of the line. The middle one shows a hyperfine structure. The results of the fit are in Table B.3. The middle panel shows the intensity maps, while the bottom panel displays the corresponding velocity maps for carbon-bearing species. From left to right, the maps represent CO in the UO band, its isotopologue $C^{17}O$ in the UO band, and $C^{18}O$ in the UI band. The velocity integration intervals are as follows: CO: $[-1.92,\ 8.48]$ km.s^{-1}, $C^{17}O$: $[3.8,\ 5.88]$ km.s^{-1}, and $C^{18}O$: $[3,\ 5.7]$ km.s^{-1}.

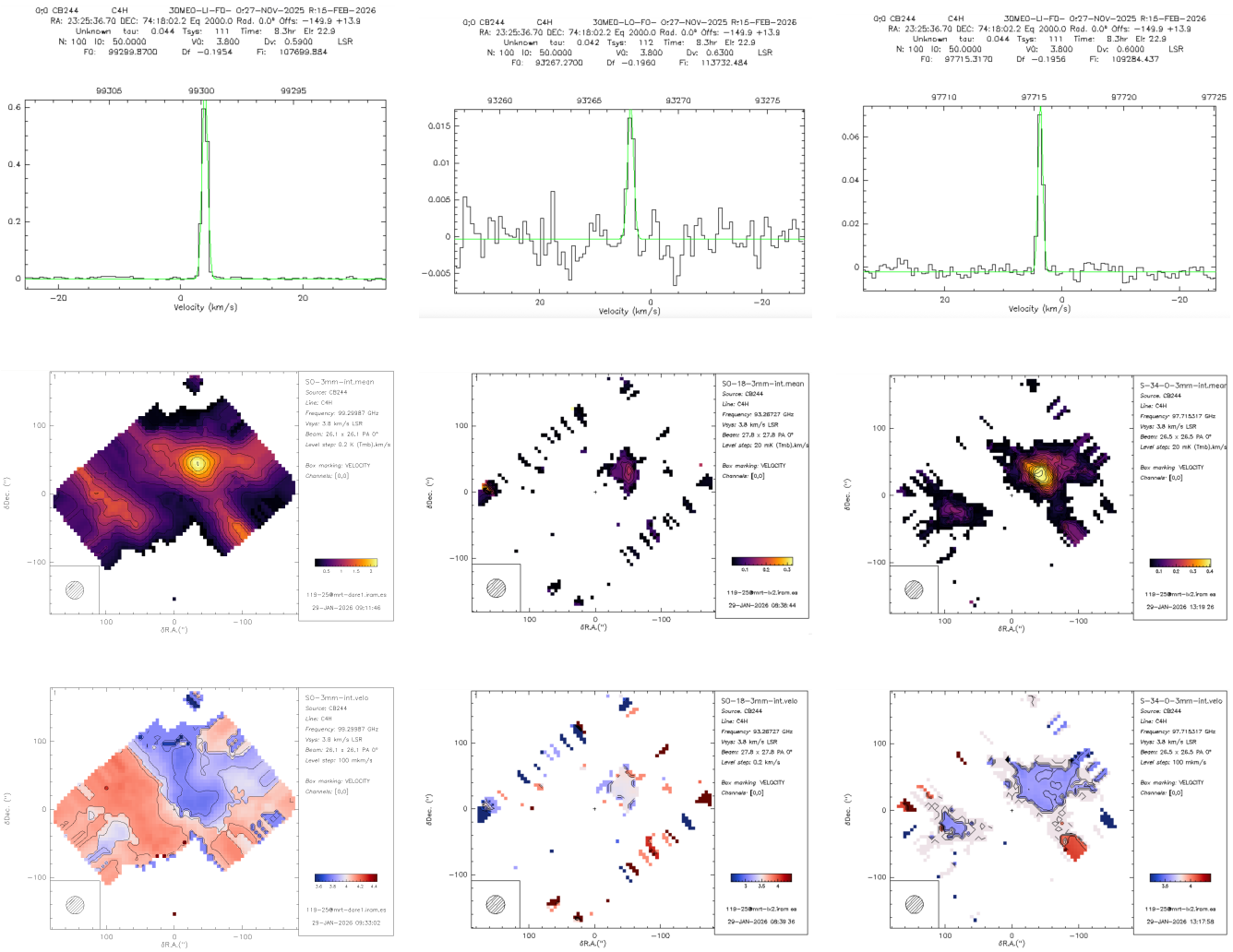

Figure A.11: The top panel shows the line with Gaussian fits and some information about the data. The results of the fit are in Table B.3. The middle panel shows the intensity maps, while the bottom panel displays the corresponding velocity maps for sulfur-bearing species. From left to right, the maps represent SO in the LI band, $S^{18}O$ in the LO band, and ^{34}SO in the LI band. The velocity integration intervals are as follows: SO: [2.62, 4.98] km.s^{-1}, ^{34}SO: [3.2, 4.4] km.s^{-1}, and $S^{18}O$: [2.54, 4.43] km.s^{-1}.

Appendix B. Tables of data

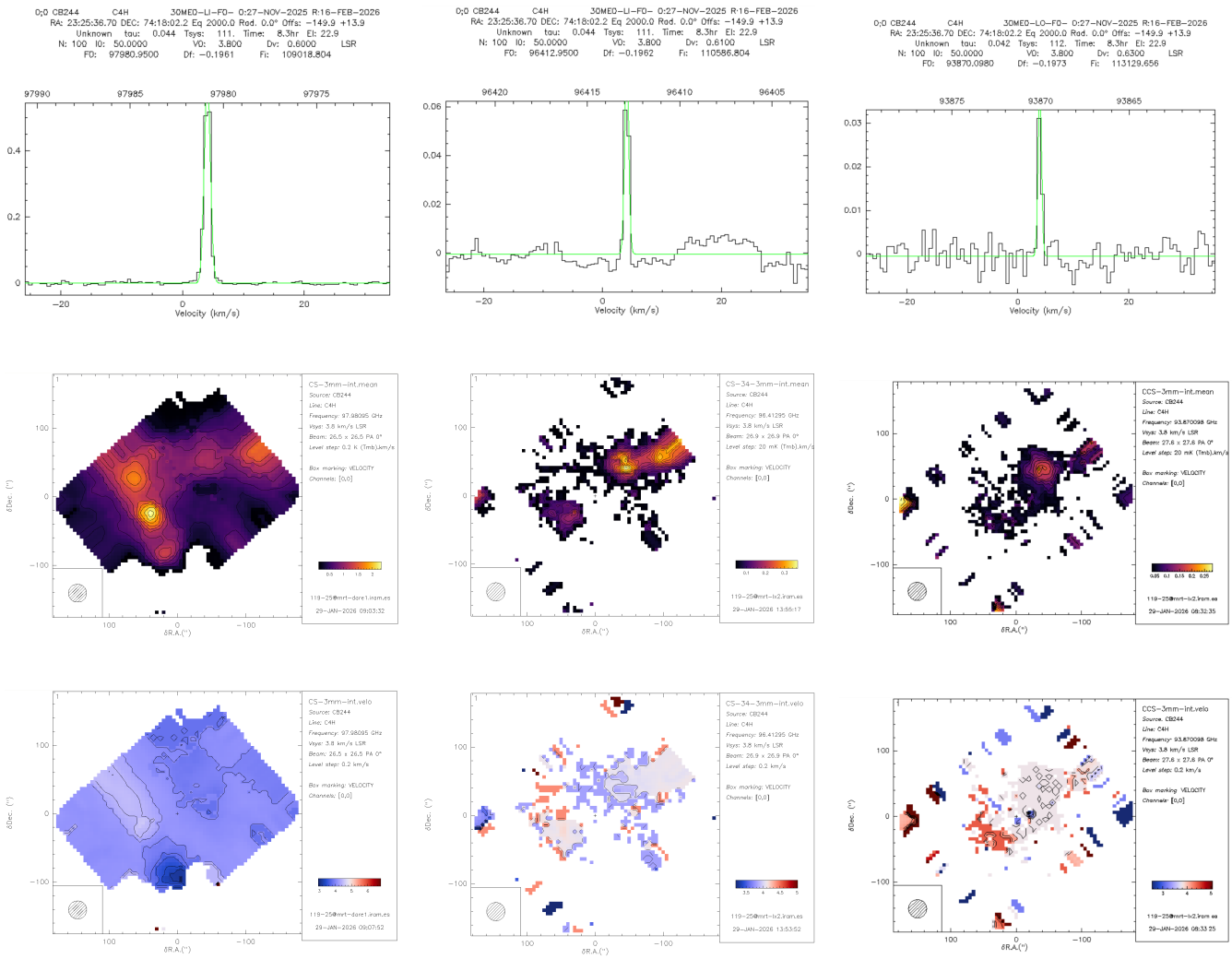

Figure A.12: The top panel shows the line with Gaussian fits and some information about the data. The middle panel shows the intensity maps, while the bottom panel displays the corresponding velocity maps for sulfur- and carbon-bearing species. The results of the fit are in Table B.3. From left to right, the maps represent CS and its isotopologue $C^{34}S$ in the LI band, and CCS in the LO band. The velocity integration intervals are as follows: CS: [2, 6.8] km.s^{-1}, $C^{34}S$: [3.19, 5.02] km.s^{-1}, and CCS: [2.54, 5.06] km.s^{-1}.

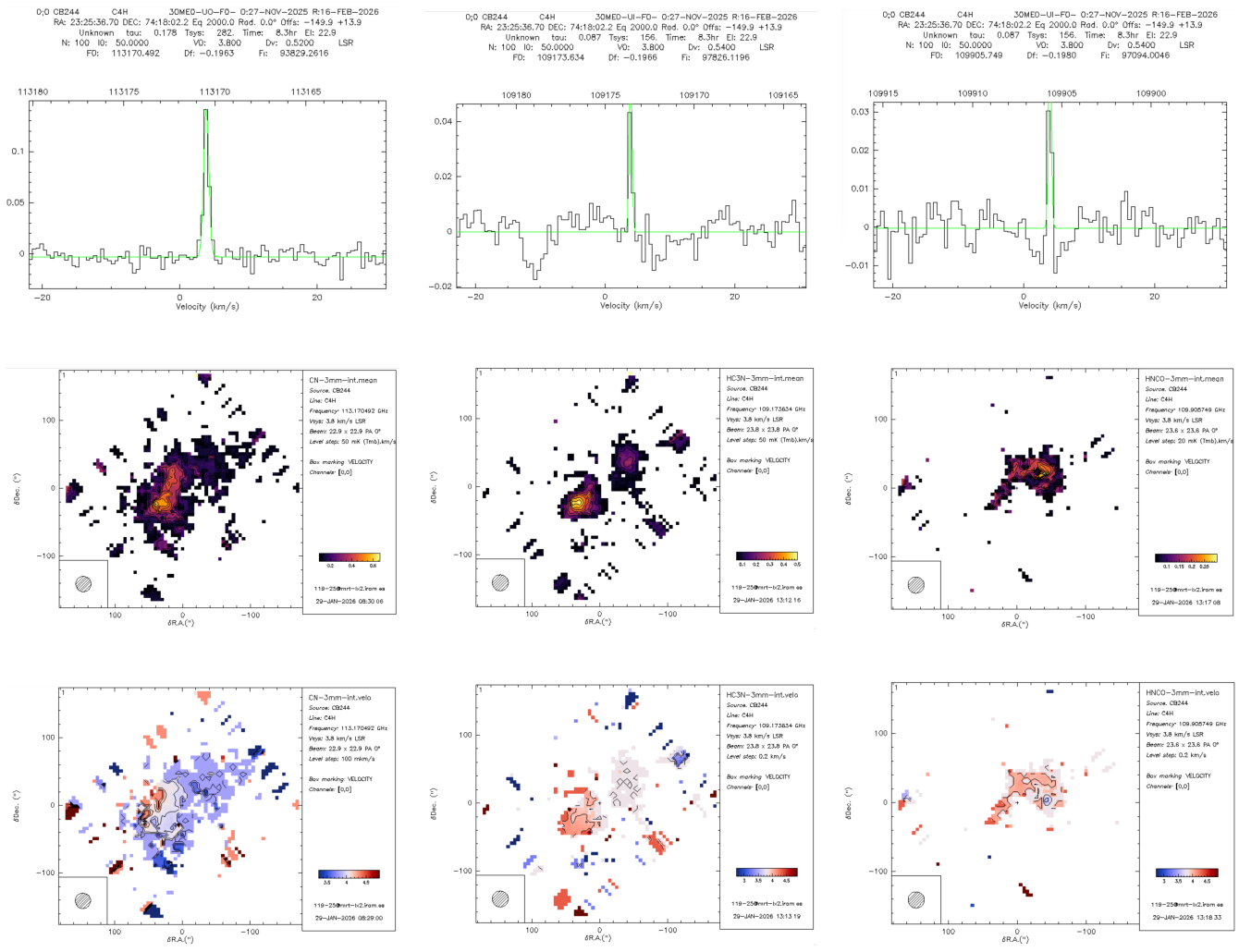

Figure A.13: The top panel shows the line with Gaussian fits and some information about the data. The results of the fit are in Table B.3. The middle panel shows the intensity maps, while the bottom panel displays the corresponding velocity maps for nitrogen- and carbon-bearing species. From left to right, the maps represent CN in the UO band, and HC_3N and HNCO in the UI band. The velocity integration intervals are as follows: CN: [3.28, 4.84] km.s^{-1}, HC_3N: [2.7, 5] km.s^{-1}, and HNCO: [2.4, 4.8] km.s^{-1}.

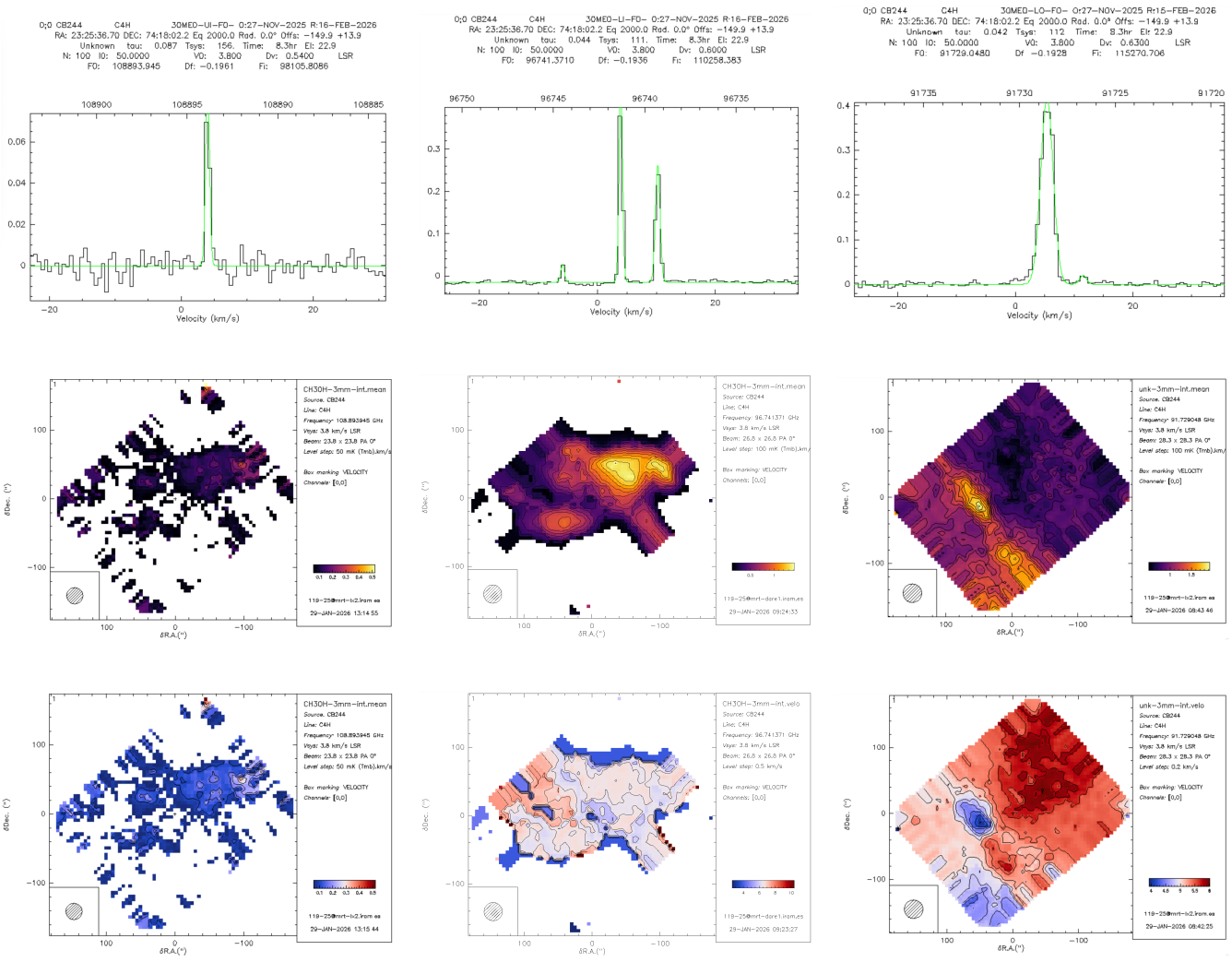

Figure A.14: The top panel shows the line with Gaussian fits and some information about the data. Again, in the middle Figure one can notice the hyperfine structure of the methanol. The results of the fit are in Table B.3. The middle panel shows the intensity maps, while the bottom panel displays the corresponding velocity maps. From left to right, the maps represent methanol in the UI band, methanol in the LI band, and an unidentified molecule in the LO band. The velocity integration intervals are as follows: CH_3OH (UI): [3.1, 5.2] km.s^{-1}, CH_3OH (LI): [2.6, 11.6] km.s^{-1}, and unidentified: [0.65, 8.21] km.s^{-1}. Further analysis showed that this unidentified line is due to a mirror effect of the CO, v=0 line that is in reality in the upper side band.

Table B.1: Observed 1 mm molecular lines in CB 244. Columns indicate the molecular species, observed base, rest frequency (MHz), measurement uncertainty (MHz), upper-state energy $E_{\rm up}$ (K), upper-state degeneracy g_u, Einstein coefficient A_{ij} (s^{-1}), transition levels $J_{\rm u} - J_{\rm l}$, and identification with the catalogue used. Finally, the degree of confidence is indicated by the column *comment*, and bands UO, UI, LI, and LO are defined in Section 2. Species marked as *Unk* have not been firmly identified in the CDMS or JPL catalogs.

Species	Band	Freq. (MHz)	Uncertainty (MHz)	$E_{\rm up}$ (K)	g_u	A_{ij} (s^{-1})	Transition	Identification
N2D+	UI	231321.828	0.004	22.2	63	$7.14e-04$	3 – 2	cdms
Unk	UI	230439	-	-	-	-	-	-
HCS+	LO	213360.650	0.020	30.7	11	$1.97e-04$	5 – 4	cdms
CH3OH, vt=0-2	LO	213427.061	0.006	23.4	12	$3.37e-05$	1 1 0 1 – 0 0 0 1	cdms
SO, v=0	LO	215220.653	0.040	44.1	11	$1.19e-04$	5 5 – 4 4	cdms
DCO+	LO	216112.582	0.005	20.7	7	$7.66e-04$	3 – 2	cdms
C-13-H3CHO	LO	216200.015	0.004	79.8	23	$6.44e-08$	11 3 8 1 – 12 012 1	cdms
Propenethial (CH2CHCHS)	LO	216212.475	0.003	73.4	41	$3.86e-06$	20 318 – 20 219	cdms
gG'a-1,2-Propanediol	LO	216219.363	0.007	85.5	41	$6.75e-06$	20 912 – 19 812	cdms
Ga-n-C3H7OH	LO	216246.889	0.100	62.3	31	$1.26e-05$	15 411 – 14 312	cdms
c-C3H2	LO	216278.756	0.021	19.5	21	$2.56e-04$	3 3 0 – 2 2 1	cdms
HOCH2C(O)NH2	LO	216324.114	0.007	67.5	33	$2.95e-04$	16 8 9 – 15 7 8	cdms
CCD	LO	216428.253	0.009	20.8	8	$2.77e-05$	3 3 4 – 2 2 3	cdms
CCD	LO	216428.431	0.009	20.8	6	$2.33e-05$	3 3 3 – 2 2 2	cdms
i-C3H7CN	LO	216750.774	0.002	56.2	33	$9.16e-06$	16 710 – 15 511	cdms
Unk	LI	221623	-	-	-	-	-	-
C-13-N	LI	217467.150	0.120	15.7	9	1.01e-04	2 3 3 4 – 1 2 2 3	cdms
C-13-N	LI	217467.150	0.120	15.7	7	8.92e-05	2 3 3 3 – 1 2 2 2	cdms
c-C3H2	LI	217822.148	0.004	38.6	13	5.40e-04	6 0 6 – 5 1 5	cdms
c-C3H2	LI	217822.148	0.004	38.6	39	5.40e-04	6 1 6 – 5 0 5	cdms
H2CCHC-13-N, v=0	LI	217821.624	0.070	25.0	51	1.40e-05	8 2 6 – 7 1 7	cdms
c-C3H2	LI	217940.046	0.007	35.4	33	4.03e-04	5 1 4 – 4 2 3	cdms
SO, v=0	LI	219949.442	0.040	35.0	13	1.34e-04	5 6 – 4 5	cdms
c-C3H2	LI	218160.456	0.002	35.4	11	4.04e-04	5 2 4 – 4 1 3	cdms
H2CO	LI	218222.192	0.010	21.0	7	2.82e-04	3 0 3 – 2 0 2	cdms
CH3OH, vt=0-2	LI	218440.063	0.013	45.5	36	4.69e-05	4 2 3 1 – 3 1 2 1	cdms
H2CO	LI	218475.632	0.010	68.1	7	1.57e-04	3 2 2 – 2 2 1	cdms
CH3CHDCN	LI	218475.914	0.008	47.3	27	2.64e-05	13 310 – 12 211	cdms
H2CO	LI	218760.066	0.010	68.1	7	1.58e-04	3 2 1 – 2 2 0	cdm
C2H5CN, v=0	LI	219463.640	0.002	112.5	45	4.29e-05	22 221 – 21 120	cdms
CO-18	LI	219560.358	0.000	15.8	5	6.01e-07	2 – 1	cdms
H2C-13-O	LI	219908.525	0.056	32.9	21	2.56e-04	3 1 2 – 2 1 1	cdms
SO, v=0	LI	219949.442	0.040	35.0	13	1.34e-04	5 6 – 4 5	cdms
C-13-O	LI	220398.684	0.000	15.9	10	6.08e-07	2 – 1	cdms
Unk	UI	229601	-	-	-	-	-	-
H2CCHO	UI	229000.616	0.005	16.8	7	2.14e-05	3 2 2 6 3 – 2 1 1 6 2	cdms
H2CCHO	UI	229000.323	0.005	16.8	9	2.24e-05	3 2 2 3 4 – 2 1 1 3 3	cdms
D2CO	UI	231410.234	0.050	27.9	18	3.47e-04	4 0 4 – 3 0 3	cdms
Unk	UO	235707.737	-	-	-	-	-	-

Table B.2: Detected 3 mm molecular lines in CB 244. The table lists the molecular species, observed base, rest frequency (MHz) with measurement uncertainty, upper-state energy $E_{\rm up}$ (K), upper-state degeneracy g_u, Einstein A coefficient A_{ij} (s^{-1}), transition levels $J_{\rm u} - J_{\rm l}$ and the map (if it is available, marked *y*), with the catalog identification. Finally, the degree of confidence is indicated by the column *comment*, and bands UO, UI, LI, and LO are defined in Section 2

Species	Band	Freq. (MHz)	Uncertainty (MHz)	$E_{\rm up}$ (K)	g_u	A_{ij} (s^{-1})	Transition	Map-Idendtification	Comment
H2CCCHCN	LO	91494.555	0.211	7.0	27	3.20e-06	4 2 2 – 3 1 3	cdms	Tentative
C-13-CP	LO	91497.137	0.051	18.4	16	4.48e-07	8-1 8 7 8 – 7 1 7 7 8	cdms	Tentative
C-13-CP	LO	91497.802	0.051	18.4	14	4.26e-07	8-1 8 7 7 – 7 1 7 7 7	cdms	Tentative
HNC(CH3)CN	LO	91496.824	0.012	50.4	35	3.22e-07	17 116 0 – 17 117 0	cdms	Tentative
HNC(CH3)CN	LO	91497.038	0.012	50.4	35	3.47e-07	17 116 0 – 17 017 0	cdms	Tentative
i-C3H7CN	LO	91729.048	0.001	36.0	27	5.96e-05	13 5 9 – 12 5 8	cdms	Unidentified
C2H3C3N	LO	91729.268	0.030	77.2	207	1.15e-04	34 034 – 33 033	cdms	Unidentified
C-13-S, v=0,1	LO	92494.308	0.050	6.7	10	1.41e-05	2 0 – 1 0	cdms	Secure
C5C-13-H	LO	93171.013	0.691	79.1	70	1.42e-04	34-1353435 – 33 1343334	cdms	Tentative
C5C-13-H	LO	93171.064	0.693	79.1	72	1.42e-04	34-1353536 – 33 1343435	cdms	Tentative
C5C-13-H	LO	93171.066	0.691	79.1	68	1.42e-04	34-1353434 – 33 1343333	cdms	Tentative
C5C-13-H	LO	93171.117	0.693	79.1	70	1.42e-04	34-1353535 – 33 1343434	cdms	Tentative
N2H+, v=0	LO	93173.398	0.001	4.5	27	3.63e-05	1 – 0	y-cdms	Secure
C7H6O	LO	93175.819	0.001	84.3	69	3.79e-05	34 430 – 33 429	cdms	Unidentified
CH3CHCCHCN	LO	93176.439	0.566	46.3	33	1.14e-06	16 7 9 – 17 612	cdms	Unidentified
CH3CHCCHCN	LO	93176.439	0.566	46.3	33	1.14e-06	16 710 – 17 611	cdms	Unidentified
SO-18	LO	93267.270	0.200	8.7	7	9.34e-06	2 3 – 1 2	cdms	Probable
CCS	LO	93870.098	0.001	19.9	17	3.74e-05	7 8 – 6 7	cdms	Probable
HCOOCH2D	LO	94062.466	0.010	8.3	9	7.40e-07	4 2 2 2 – 3 1 3 2	cdms	Tentative
C-13-H3C-13-H2CN, v=0	LO	94062.595	0.001	27.3	23	6.85e-05	11 011 – 10 010	cdms	Tentative
SiCN	LO	94064.214	0.003	21.2	18	5.31e-07	9 1 9 9 – 8-1 8 9	cdms	Tentative
Cyclopropenone-1D	LO	94921.580	0.005	27.4	15	7.31e-05	7 3 4 – 6 3 3	cdms	Tentative
c-CD2CH2O	LO	94921.598	0.000	41.2	15	2.92e-06	7 2 6 – 7 1 7	cdms	Tentative
CH3COOH, vt=0	LO	94921.838	0.001	46.0	23	8.48e-08	11 2 9 0 2 – 11 210 0 1	cdms	Probable
CH3COOH, vt=0	LO	94921.839	0.001	46.0	23	3.86e-07	11 2 9 0 2 – 11 110 0 1	cdms	Probable
CH3COOH, vt=0	LO	94921.913	0.001	46.0	23	3.86e-07	11 3 9 0 2 – 11 210 0 1	cdms	Probable
CH3COOH, vt=0	LO	94921.914	0.001	46.0	23	8.48e-08	11 3 9 0 2 – 11 110 0 1	cdms	Probable
c-C2H3(O)CN	LO	94922.101	0.003	12.1	15	3.90e-06	7 2 6 – 6 1 6	cdms	Tentative
OCS-34	LO	94922.799	0.002	20.5	17	2.40e-06	8 – 7	cdms	Probable
C4H, v=0	LO	95150.389	0.003	25.1	21	2.10e-05	101110 – 910 9	cdms	Probable
C4H, v=0	LO	95150.398	0.003	25.1	23	2.11e-05	101111 – 91010	cdms	Probable
C4H, v=0	LO	95188.947	0.003	25.1	19	2.08e-05	1010 9 – 9 9 8	cdms	Probable
C4H, v=0	LO	95188.949	0.003	25.1	21	2.10e-05	101010 – 9 9 9	cdms	Probable
CS-34, v=0,1	LI	96412.950	0.002	6.9	5	1.60e-05	2 0 – 1 0	y-cdms	Probable
HCOCN	LI	96413.547	0.004	25.5	21	1.12e-05	10 010 – 9 0 9	cdms	Probable
CH3OH$^{\alpha}$ vt=0-2	LI	96739.358	0.002	12.5	20	2.56e-06	2 1 2 2 – 1 1 1 2	y-cdms	Secure
CH3OH$^{\alpha}$, vt=0-2	LI	96741.371	0.002	7.0	20	3.41e-06	2 0 2 0 – 1 0 1 0	y-cdms	Probable
CH3OCCH	LI	96742.272	0.016	11.0	9	4.38e-06	4 2 2 0 – 4 1 3 0	cdms	Probable
CH3CHCCHCN	LI	96744.516	0.053	11.7	13	7.47e-06	6 4 3 – 5 3 2	cdms	Not sure
CH3CHCCHCN	LI	96744.516	0.053	11.7	13	4.64e-07	6 4 2 – 5 3 2	cdms	Not sure
CH3OH$^{\alpha}$, vt=0-2	LI	96744.545	0.002	20.1	20	3.41e-06	2 0 2 1 – 1 0 1 1	y-cdms	Probable
CH3CHCCHCN	LI	96744.568	0.053	11.7	13	4.64e-07	6 4 3 – 5 3 3	cdms	Not sure
CH3CHCCHCN	LI	96744.568	0.053	11.7	13	7.47e-06	6 4 2 – 5 3 3	cdms	Not sure
CH3C(O)NH2, vt=1	LI	96797.546	0.011	54.7	15	1.73e-05	7 2 5-2 – 6 3 4-2	cdms	Tentative
Indene	LI	96799.038	0.002	22.2	33	1.55e-08	16 611 – 15 312	y-cdms	Tentative
OCS, v=0	LI	97301.208	0.000	21.0	17	2.58e-06	8 – 7	y-cdms	Probable
S-34-O	LI	97715.317	0.050	9.1	7	1.07e-05	2 3 – 1 2	y-cdms	Secure
CS, v=0-4	LI	97980.953	0.002	7.1	5	1.68e-05	2 0 – 1 0	y-cdms	Secure
SO, v=0	LI	99299.870	0.100	9.2	7	1.13e-05	2 3 – 1 2	y-cdms	Secure
CO-18	UI	109782.176	0.000	5.3	3	6.27e-08	1 – 0	cdms	Secure
SO, v=0	UI	109252.220	0.100	21.1	5	1.08e-05	3 2 – 2 1	cdms	Secure
HC3N, v=0	UI	109173.634	0.010	34.1	25	1.01e-04	12 – 11	cdms	Probable
C-13-O	UI	110201.354	0.000	5.3	6	6.33e-08	1 – 0	cdms	Secure
CH3OH, vt=0-2	UI	108893.945	0.012	13.1	4	1.47e-05	0 0 0 1 – 1 1 1 2	y-cdms	Secure
HNCO	UI	109905.749	0.007	15.8	11	1.75e-05	5 0 5 – 4 0 4	cdms	Probable
CO-17	UO	112359.285	0.000	5.4	18	6.70e-08	1 – 0	cdms	Secure
CN, v=0,1	UO	113123.370	0.006	5.4	2	1.29e-06	1 0 1 1 – 0 0 1 1	cdms	Probable
CN, v=0,1	UO	113144.157	0.006	5.4	2	1.05e-05	1 0 1 1 – 0 0 1 2	cdms	Probable
CN, v=0,1	UO	113170.492	0.004	5.4	4	5.15e-06	1 0 1 2 – 0 0 1 1	cdms	Probable
CN, v=0,1	UO	113191.279	0.003	5.4	4	6.68e-06	1 0 1 2 – 0 0 1 2	cdms	Probable
HNC(CH3)CN	UO	113477.642	0.011	19.9	17	2.53e-06	8 5 3 0 – 7 4 4 0	cdms	Tentative
CH3CDO, vt=0,1	UO	113478.134	0.010	46.4	13	2.75e-05	6 4 3 0 – 5 4 2 0	cdms	Probable
CN, v=0,1	UO	113488.120	0.003	5.4	4	6.74e-06	1 0 2 2 – 0 0 1 1	cdms	Probable
CN, v=0,1	UO	113490.970	0.002	5.4	6	1.19e-05	1 0 2 3 – 0 0 1 2	cdms	Probable
CN, v=0,1	UO	113499.644	0.003	5.4	2	1.06e-05	1 0 2 1 – 0 0 1 1	cdms	Probable
CN, v=0,1	UO	113508.907	0.003	5.4	4	5.19e-06	1 0 2 2 – 0 0 1 2	cdms	Probable
CN, v=0,1	UO	113520.432	0.004	5.4	2	1.30e-06	1 0 2 1 – 0 0 1 2	cdms	Probable
CO, v=0	UO	115271.202	0.001	5.5	3	7.20e-08	1 – 0	cdms	Secure

[1]The CH_3OH lines labeled with $^{\alpha}$ correspond to three closely spaced transitions in the torsional ground state ($v_t = 0$) detected in the LI band.

Table B.3: Results of the Gaussian fits on the emission lines

Species	Area [km.s^{-1}.K]	Position [km.s^{-1}]	Width [km.s^{-1}]	T_{peak} [K]
CH_3OH	$3.15 \times 10^{-2} \pm 3.22 \times 10^{-3}$	-5.888 ± 0.059	0.705 ± 0.089	4.20×10^{-2}
CH_3OH	$0.3496 \pm 2.94 \times 10^{-3}$	3.971 ± 0.005	0.713 ± 0.014	0.4605
CH_3OH	$0.2713 \pm 3.41 \times 10^{-3}$	10.242 ± 0.006	0.924 ± 0.014	0.2758
CS	$0.7768 \pm 4.85 \times 10^{-3}$	4.072 ± 0.004	1.200 ± 0.009	0.6081
$C^{34}S$	$6.94 \times 10^{-2} \pm 4.51 \times 10^{-3}$	4.061 ± 0.030	0.823 ± 0.131	7.92×10^{-2}
^{34}SO	$7.84 \times 10^{-2} \pm 2.53 \times 10^{-3}$	3.670 ± 0.017	0.968 ± 0.036	7.61×10^{-2}
SO	$0.7783 \pm 3.50 \times 10^{-3}$	3.985 ± 0.003	1.107 ± 0.006	0.6603
CCS	$3.00 \times 10^{-2} \pm 3.00 \times 10^{-3}$	3.983 ± 0.069	0.759 ± 0.179	3.71×10^{-2}
N_2H^+	$0.1594 \pm 3.41 \times 10^{-3}$	-5.171 ± 0.009	0.848 ± 0.020	0.1767
N_2H^+	$0.642 \pm 4.46 \times 10^{-3}$	3.043 ± 0.007	1.802 ± 0.010	0.335
N_2H^+	$0.41 \pm 3.14 \times 10^{-3}$	8.727 ± 0.008	1.525 ± 0.008	0.251
$S^{18}O$	$2.48 \times 10^{-2} \pm 3.10 \times 10^{-3}$	3.627 ± 0.082	1.291 ± 0.176	1.80×10^{-2}
unk	$1.11 \pm 5.85 \times 10^{-3}$	5.837 ± 0.009	2.521 ± 0.004	0.416
unk	$2.96 \times 10^{-2} \pm 6.79 \times 10^{-3}$	11.533 ± 0.150	1.421 ± 0.447	1.959×10^{-2}
^{13}CO	0.43 ± 0.51	-1.165 ± 0.510	2.034 ± 0.510	0.197
^{13}CO	11.07 ± 0.51	3.821 ± 0.510	1.953 ± 0.510	5.322
$C^{18}O$	$1.03 \pm 3.35 \times 10^{-3}$	4.018 ± 0.002	1.003 ± 0.004	0.9681
CH3OH	$6.67 \times 10^{-2} \pm 4.58 \times 10^{-3}$	4.008 ± 0.024	0.718 ± 0.117	8.73×10^{-2}
HC_3N	$3.19 \times 10^{-2} \pm 6.37 \times 10^{-3}$	3.960 ± 0.049	0.545 ± 0.809	55.497×10^{-2}
HNCO	$2.86 \times 10^{-2} \pm 3.87 \times 10^{-3}$	4.0277 ± 0.026	0.540 ± 0.414	4.979×10^{-2}
CN	$0.14 \pm 7.19 \times 10^{-3}$	3.867 ± 0.023	0.897 ± 0.053	0.144
CO	0.36 ± 0.50	-1.058 ± 0.520	1.947 ± 0.520	0.172
CO	11.02 ± 0.50	3.815 ± 0.520	1.939 ± 0.520	5.338
$C^{17}O$	$0.11 \pm 7.17 \times 10^{-3}$	2.092 ± 0.029	0.888 ± 0.077	0.112
$C^{17}O$	$0.22 \pm 7.77 \times 10^{-3}$	4.912 ± 0.018	1.100 ± 0.047	0.190

Appendix C. Spectrum

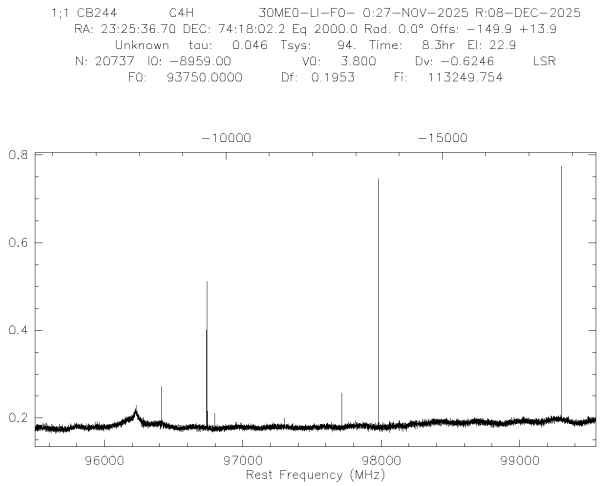

(a) Lower Sideband – Inner window (LI)

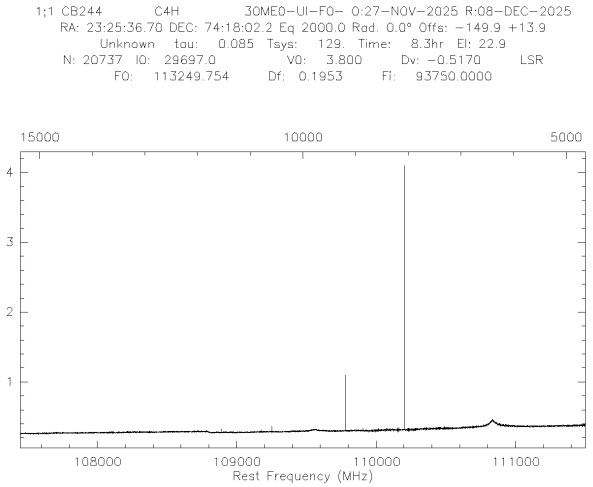

(b) Upper Sideband – Inner window (UI)

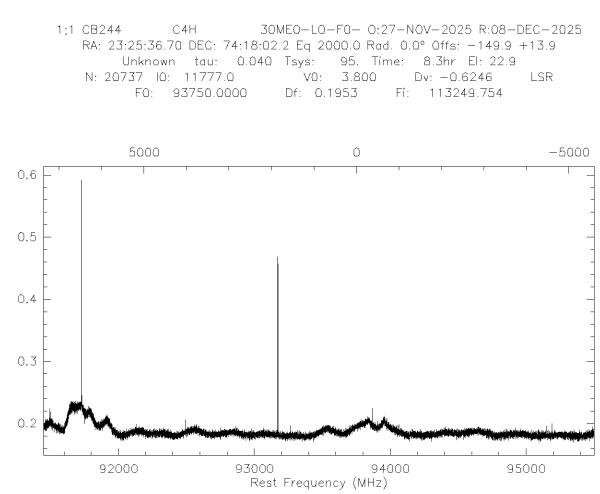

(c) Lower Sideband – Outer window (LO)

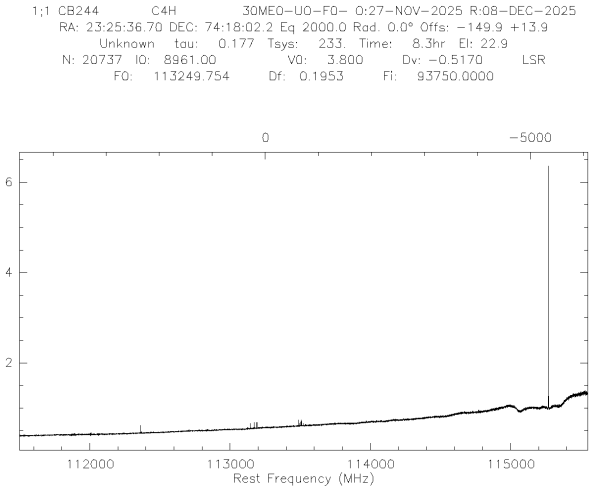

(d) Upper Sideband – Outer window (UO)

Figure C.15: Spectral coverage obtained with the IRAM 30 m telescope using the EMIR receiver in dual-sideband mode. The four panels show the inner and outer spectral windows of the lower and upper sidebands (LSB/USB) for a single tuning.

References

Bergin, E.A., Tafalla, M., 2007. Cold dark clouds: The initial conditions for star formation. Annual Review of Astronomy and Astrophysics 45, 339–396. URL: http://dx.doi.org/10.1146/annurev.astro.45.071206.100404, doi:10.1146/annurev.astro.45.071206.100404.

Bulut, N., Roncero, O., Aguado, A., Loison, J.-C., Navarro-Almaida, D., Wakelam, V., Fuente, A., Roueff, E., Le Gal, R., Caselli, P., Gerin, M., Hickson, K. M., Spezzano, S., Riviére-Marichalar, P., Alonso-Albi, T., Bachiller, R., Jiménez-Serra, I., Kramer, C., Tercero, B., Rodriguez-Baras, M., García-Burillo, S., Goicoechea, J. R., Treviño-Morales, S. P., Esplugues, G., Cazaux, S., Commercon, B., Laas, J., Kirk, J., Lattanzi, V., Martín-Doménech, R., Muñoz-Caro, G., Pineda, J., Ward-Thompson, D., Tafalla, M., Marcelino, N., Malinen, J., Friesen, R., Giuliano, B. M., Agúndez, M., Hacar, A., 2021. Gas phase elemental abundances in molecular clouds (gems) - iii. unlocking the cs chemistry: the cs+o reaction. AA 646, A5. URL: https://doi.org/10.1051/0004-6361/202039611, doi:10.1051/0004-6361/202039611.

Caselli, P., Ceccarelli, C., 2012. Our astrochemical heritage. The Astronomy and Astrophysics Review 20. URL: http://dx.doi.org/10.1007/s00159-012-0056-x, doi:10.1007/s00159-012-0056-x.

Caselli, P., Walmsley, C.M., Zucconi, A., Tafalla, M., Dore, L., Myers, P.C., 2002. Molecular ions in l1544. i. kinematics. The Astrophysical Journal 565, 331. URL: https://doi.org/10.1086/324301, doi:10.1086/324301.

Ceccarelli, C., et al. (Eds.), 2023. Protostars and Planets VII.

Ceccarelli, C., Caselli, P., Bockelée-Morvan, D., Mousis, O., Pizzarello, S., Robert, F., Semenov, D., 2014. Deuterium Fractionation: The Ariadne's Thread from the Precollapse Phase to Meteorites and Comets Today. University of Arizona Press. URL: http://dx.doi.org/10.2458/azu_uapress_9780816531240-ch037, doi:10.2458/azu_uapress_9780816531240-ch037.

Ceccarelli, C., Codella, C., Balucani, N., Bockelée-Morvan, D., Herbst, E., Vastel, C., Caselli, P., Favre, C., Lefloch, B., Öberg, K., 2022. Organic chemistry in the first phases of solar-type protostars. URL: https://arxiv.org/abs/2206.13270, arXiv:2206.13270.

Heithausen, A., Böttner, C., Walter, F., 2008. Chemical and physical small-scale structure in a pre-stellar core. Astronomy amp; Astrophysics 488, 597–603. URL: http://dx.doi.org/10.1051/0004-6361:20078557, doi:10.1051/0004-6361:20078557.

Herpin, F., Marseille, M., Wakelam, V., Bontemps, S., Lis, D. C., 2009. S-bearing molecules in massive dense cores ***. AA 504, 853–867. URL: https://doi.org/10.1051/0004-6361/200811257, doi:10.1051/0004-6361/200811257.

Jørgensen, J. K., Schöier, F. L., van Dishoeck, E. F., 2004. Molecular inventories and chemical evolution of low-mass protostellar envelopes*. AA 416, 603–622. URL: https://doi.org/10.1051/0004-6361:20034440, doi:10.1051/0004-6361:20034440.

Koley, A., 2022. Studying the chemical and kinematical structures of dense cores tmc-1c, l1544, and tmc-1 in the taurus molecular cloud using ccs and nh3 observations. Monthly Notices of the Royal Astronomical Society 516, 185–196. URL: http://dx.doi.org/10.1093/mnras/stac1935, doi:10.1093/mnras/stac1935.

Kutner, M.L., Ulich, B.L., 1981. Recommendations for calibration of millimeter-wavelength spectral line data. 250, 341–348. doi:10.1086/159380.

Langer, W.D., Penzias, A.A., 1993. 12C/ 13C Isotope Ratio in the Local Interstellar Medium from Observations of 13C 18O in Molecular Clouds. 408, 539. doi:10.1086/172611.

Launhardt, R., Nutter, D., Ward-Thompson, D., Bourke, T.L., Henning, T., Khanzadyan, T., Schmalzl, M., Wolf, S., Zylka, R., 2010. Looking into the hearts of bok globules: Millimeter and submillimeter continuum images of isolated star-forming cores. The Astrophysical Journal Supplement Series 188, 139–177. URL: http://dx.doi.org/10.1088/0067-0049/188/1/139, doi:10.1088/0067-0049/188/1/139.

Marcelino, N., Brünken, S., Cernicharo, J., Quan, D., Roueff, E., Herbst, E., Thaddeus, P., 2010. The puzzling behavior of hnco isomers in molecular clouds*. AA 516, A105. URL: https://doi.org/10.1051/0004-6361/200913806, doi:10.1051/0004-6361/200913806.

Marchand, P., Coutens, A., Scigliuto, J., de Miera, F. Cruz-Sáenz, Andreu, A., Loison, J.-C., Kóspál, Á., Ábráham, P., 2024. Chemical inventory of the envelope of the class i protostar l1551 irs 5. AA 687, A195. URL: https://doi.org/10.1051/0004-6361/202450023, doi:10.1051/0004-6361/202450023.

Martinez, N.C., Paron, S., Ortega, M.E., Petriella, A., Álamo, A., Brook, M., Carballo, C., Heberling, T., 2024. Sulfur-bearing molecules in a sample of early star-forming cores. Astronomy amp; Astrophysics 692, A97. URL: http://dx.doi.org/10.1051/0004-6361/202452350, doi:10.1051/0004-6361/202452350.

Müller, H.S., Schlöder, F., Stutzki, J., Winnewisser, G., 2005. The cologne database for molecular spectroscopy, cdms: a useful tool for astronomers and spectroscopists. Journal of Molecular Structure 742, 215–227. URL: https://www.sciencedirect.com/science/article/pii/S0022286005000888, doi:https://doi.org/10.1016/j.molstruc.2005.01.027. mOLECULAR SPECTROSCOPY AND STRUCTURE.

Nagaoka, A., Watanabe, N., Kouchi, A., 2005. H-d substitution in interstellar solid methanol: A key route for d enrichment. The Astrophysical Journal 624, L29. URL: https://doi.org/10.1086/430304, doi:10.1086/430304.

Pardo, J., Cernicharo, J., Serabyn, E., 2001. Atmospheric transmission at microwaves (atm): an improved model for millimeter/submillimeter applications. IEEE Transactions on Antennas and Propagation 49, 1683–1694. doi:10.1109/8.982447.

Pineda, J.E., Caselli, P., Goodman, A.A., 2008. CO Isotopologues in the Perseus Molecular Cloud Complex: the X-factor and Regional Variations. 679, 481–496. doi:10.1086/586883, arXiv:0802.0708.

Sakai, N., Sakai, T., Hirota, T., Yamamoto, S., 2008. Abundant Carbon-Chain Molecules toward the Low-Mass Protostar IRAS 04368+2557 in L1527. 672, 371–381. doi:10.1086/523635.

Sakai, N., Yamamoto, S., 2013. Warm carbon-chain chemistry. Chemical Reviews 113, 8981–9015. doi:10.1021/cr4001308.

Saury, G., Bariosco, V., Ceccarelli, C., López-Sepulcre, A., Chahine, L., Simone, M.D., Rimola, A., Ugliengo, P., Chandler, C.J., Sakai, N., Codella, C., Bianchi, E., Boitard-Crépeau, L., Bouvier, M., Gal, R.L., Loinard, L., Oya, Y., Podio, L., Sabatini, G., Vastel, C., Zhang, Z.E., Yamamoto, S., 2025. Faust xxix. ocs line emission: a new method for measuring the luminosity of embedded protostars in binary systems. URL: https://arxiv.org/abs/2512.04674, arXiv:2512.04674.

Spezzano, S., Sipilä, O., Caselli, P., 2016. Understanding the c3h2cyclic-to-linear ratio in l1544. Astronomy amp; Astrophysics 591, L1. URL: http://dx.doi.org/10.1051/0004-6361/201628689, doi:10.1051/0004-6361/201628689.

Stutz, A., Launhardt, R., Linz, H., Krause, O., Henning, T., Kainulainen, J., Nielbock, M., Steinacker, J., André, P., 2010. Dust-temperature of an isolated star-forming cloud: Herschel observations of the bok globule cb244*. AA 518, L87. URL: https://doi.org/10.1051/0004-6361/201014537, doi:10.1051/0004-6361/201014537.

Ulich, B.L., Haas, R.W., 1976. Absolute calibration of millimeter-wavelength spectral lines. 30, 247–258. doi:10.1086/190361.

Wilson, T.L., Rood, R., 1994. Abundances in the Interstellar Medium. 32, 191–226. doi:10.1146/annurev.aa.32.090194.001203.

Zamirri, L., Ugliengo, P., Ceccarelli, C., Rimola, A., 2019. Quantum mechanical investigations on the formation of complex organic molecules on interstellar ice mantles. review and perspectives. ACS Earth and Space Chemistry 3, 1499–1523. URL: https://doi.org/10.1021/acsearthspacechem.9b00082, doi:10.1021/acsearthspacechem.9b00082, arXiv:https://doi.org/10.1021/acsearthspacechem.9b00082.